Angular momentum induced delays in solid state photoemission enhanced by intra-atomic interactions

Fabian Siek[1], Sergej Neb[1], Peter Bartz[1], Matthias Hensen[1], Christian Strüber[1 †],

Sebastian Fiechter[2], Miquel Torrent-Sucarrat[3,4,5], Vyacheslav M. Silkin[3,4,5],

Eugene E. Krasovskii[3,4,5], Nikolay M. Kabachnik[6,7], Stephan Fritzsche[8],

Ricardo Díez Muiño[4,9], Pedro M. Echenique[3,4,9], Andrey K. Kazansky[3,4,5], Norbert Müller[1],

Walter Pfeiffer[1*], Ulrich Heinzmann[1]

[1]Fakultät für Physik, Universität Bielefeld, Universitätsstr. 25, 33615 Bielefeld, Germany.

[2]Institut für Solare Brennstoffe, Helmholtz-Zentrum Berlin für Materialien und Energie GmbH,

Hahn-Meitner-Platz 1, 14109 Berlin, Germany.

[3]University of the Basque Country, 20080 San Sebastián, Spain.

[4]Donostia International Physics Center (DIPC), 20018 San Sebastián, Spain.

[5]IKERBASQUE, Basque Foundation for Science, 48013 Bilbao, Spain.

[6]Skobeltsyn Institute of Nuclear Physics, Lomonosov Moscow State University,

Moscow 119991, Russia.

[7]European XFEL GmbH, Holzkoppel 4, 22869 Schenefeld, Germany.

[8]Helmholtz-Institut Jena, Fröbelstieg 3, 07743 Jena, Germany.

[9]Centro de Física de Materiales CFM/MPC (CSIC-UPV/EHU), 20018 San Sebastián, Spain.

*Correspondence to: pfeiffer@physik.uni-bielefeld.de

[†] present address: Max Born Institute for Nonlinear Optics and Short Pulse Spectroscopy

in the Forschungsverbund Berlin e.V., Max-Born-Straße 2 A, 12489 Berlin, Germany.

Abstract: Attosecond time-resolved photoemission spectroscopy reveals that photoemission from solids is not yet fully understood. The relative emission delays between four photoemission channels measured for the van der Waals crystal WSe_2 can only be explained by accounting for, both, propagation and intra-atomic delays. The intra-atomic delay depends on the angular momentum of the initial localized state and is determined by intra-atomic interactions. For the studied case of WSe_2 the photoemission events are time-ordered with rising initial state angular momentum. Including intra-atomic electron-electron interaction and angular momentum of the initial localized state yields excellent agreement between theory and experiment. This has required a revision of existing models for solid state photoemission and, thus, attosecond time-resolved photoemission from solids provides important benchmarks for improved future photoemission models.

One Sentence Summary: Attosecond time-resolved spectroscopy reveals angular momentum induced delays in solid state photoemission and is thereby revising common photoemission models.

Photoemission spectroscopy is widely used to study electronic properties of solids. The momentum and energy distribution of photoelectrons reflects the electronic ground state and is well understood based on theoretically derived electronic ground state configurations and delocalized photoemission states. However, as demonstrated here, the dynamics of the photoemission process is not correctly captured in common models of solid state photoemission. In the very initial stage of the photoemission process the excited state dynamics is governed by

the local environment, i.e. the inner configuration of the atom. This gives rise to an angular momentum dependent delay that is enhanced by intra-atomic interactions (upper left panel in Fig. 1 and Supplementary Materials section 2.1). These effects are well established for the photoemission from atoms (*1–4*) but are neglected in models of solid state photoemission. Realistic modelling photoelectron kinematics and photoemission delays thus requires a revision of these models, i.e., both intra-atomic delays and propagation effects must be considered (upper panels in Fig. 1).

The reported results are based on attosecond time-resolved photoemission spectroscopy using the streaking approach (*5*). As depicted in Fig. 1 the photoelectron excited by an attosecond EUV pulse is exposed to an IR streaking field. The delay t_{IR} - t_{EUV} between IR and EUV pulse and the photoemission delay, i.e. the time until the photoelectron leaves the solid and feels the streaking field, determine the streaking signal (*5*) and the streaking spectrogram yields delay differences between the various emission channels. WSe_2 is chosen as substrate since the photoemission spectrum for the EUV photon energy (Fig. 2A) is dominated by four emission channels with different initial state characteristics: A valence band (VB) emission (E_{kin} = 87.0 eV) and photoemission from the Se 4s, W 4f, and Se 3d core levels at E_{kin} = 73.5 eV, E_{kin} = 54.2 eV, and E_{kin} = 32.2 eV (*6*), respectively. WSe_2 (Fig. 1) allows in-situ cleaving and yields rather inert surfaces. Its layered structure helps identifying from which depth a particular photoelectron is emitted. Together with the minimization of systematic errors induced by chirp of the EUV pulse (< 0.01 fs^2) and magnetic fields (< 1 µT) to less than 2 as this allows determining relative photoemission delays with 10 as resolution.

From fitting the background corrected spectra recorded for different delay $t_{IR} - t_{EUV}$ the delay-dependent energy positions of four spectral components were determined (Fig. 2B).

Simultaneous fitting (continuous lines in the overlay in Fig. 2B) of these streaking curves yields

the photoemission delays Δt and the corresponding relative photoemission delays $\Delta t_{\mathrm{VB-Se\,4s}}$,

$\Delta t_{\mathrm{Se\,3d-Se\,4s}}$, and $\Delta t_{\mathrm{W\,4f-Se\,4s}}$ relative to the emission from the Se 4s core level. The latter are shown

in the left part of Fig. 3 as function of time after cleaving. Within the experimental uncertainties

the delays show no systematic variation. Consequently, the individual measurements are

averaged and small statistical uncertainties of about 10 as are achieved for the three different

relative delays (red data points in the right part of Fig. 3). Note that averaging over different sub-

ensembles (see Supplementary Materials section 1.3 for details) does not significantly alter the

retrieved average relative delays. In addition, ambiguities in the delay determination arising from

various data evaluation procedures are excluded. Five different background subtraction

procedures (see Supplementary Materials Fig. S1B) yield within the statistical uncertainty the

same relative delays (right part of Fig. 3). As systematic errors are negligible, the error margins

for the experimentally determined photoemission delays noted in the right part of Fig. 3 and

tabulated in Tab. 1 reflect the counting statistics of individual streaking spectra, the scattering of

results for different WSe$_2$ crystals, different positions on the cleaved surfaces, and ambiguities of

the evaluation procedure.

The positive relative delays indicate a photoemission sequence as follows: The photoelectrons

emitted from the Se 4s state arrive first, about 10 as later the electrons from the VB

($\Delta t_{\mathrm{VB-Se\,4s}} = 12 \pm 10\,\mathrm{as}$), and again roughly 20 as later photoelectrons originating from the Se 3d

core level appear ($\Delta t_{\mathrm{Se\,3d-Se\,4s}} = 28 \pm 10\,\mathrm{as}$). Finally, the electrons from the W 4f state arrive again

about 20 as later ($\Delta t_{\mathrm{W\,4f-Se\,4s}} = 47 \pm 14\,\mathrm{as}$). This emission sequence has a striking qualitative

behavior: the emission events appear time-ordered with respect to rising angular momentum of

the initial states. Emission from Se 4s is fastest although the kinetic energy of the photoelectrons is lower than for the VB emission and is thus expected to proceed slower. The emission from the state with the highest angular momentum, i.e. the W 4f state, is last. Electrons originating from Se 3d have a lower kinetic energy but are emitted earlier. Assignment of an angular momentum to the VB is difficult, but the bonding in WSe_2 is dominated by Se 4p- and W 5d-orbitals (Supplementary Material section 2.2) and thus also the VB emission is matching this pattern of increasing delay with increasing angular momentum. This time-ordering according to initial state angular momenta provides a first hint that intra-atomic effects (Fig. 1) affect the photoemission kinematics. However, the effects are subtle and a theoretical analysis accounting for known effects influencing the photoemission delay is needed to clearly identify the underlying mechanisms.

Table 1 summarizes the measured delays and compares them to theory. A full three-dimensional quantum mechanical model that accounts for the transient many-body effects is still beyond the reach of the contemporary theoretical methods. Here we separate the photoemission process into two steps, i.e. an intra-atomic initial stage and the propagation in an effective one-dimensional potential in the solid, as they are indicated in the upper panels in Fig. 1.

The intra-atomic delays summarized in Tab. 1 are derived using, both, an independent electron Hartree-Slater (HS) model (7) and the Multiconfiguration Dirac-Fock (MCDF) approach (8) which accounts for electron correlations and relativistic effects (Supplementary Materials section 2.1). Both methods consistently yield relative delays that become larger with increasing angular momentum difference to the Se 4s state. In contrast to the MCDF calculations, the HS method provides an intuitive interpretation of the intra-atomic effects enhancing the photoemission delays (upper left panel in Fig. 1 and Supplementary Material section 2.1.3): The electron-

electron interaction within the atom screens the Coulomb interaction with the nucleus and is taken into account in a single particle approach by the spherically symmetric Hartree-Slater potential $U^{HS}(r)$. The effective potential $U^{HS}_{eff}(r) = U^{HS}(r) + l(l+1)/2r^2$ (in a.u.) that combines electrostatic attraction and centrifugal repulsion governs the photoelectron dynamics. In time-resolved experiments performed on atoms (*2*) and molecules (*9*) this mechanism is well established and accounted for in theoretical modelling of photoemission delays (*4*). For high angular momenta $l \geq 2$, the complicated shape of the effective potential strongly varies with atomic number Z (*10*). Such an *l*-dependent effective potential determines the photoelectron phase shift (and time delay), which includes the impact of intra-atomic interactions. Accordingly, the time delay depends on *l* and thus on the electron angular momentum in the initial atomic state (see Supplementary Materials section 2.1 for details). The impact of the centrifugal term increases with increase of *l* and is most pronounced in the core of the atom where charge screening is most effective, i.e. for radii smaller than about 1 Å. Thus the corresponding delay is accumulated in the very initial stage of the photoemission process. This strong localization allows separating the photoemission process in an intra-atomic initial step and the subsequent propagation in the solid.

The photoelectron propagation in the solid and the emission is modeled using a single-particle time-dependent Schrödinger equation approach (TDSE) (*11*, *12*). The method originally developed for gas phase streaking (*13*) is adapted here to account for the streaking field distribution, the inner potential of WSe_2 (*14*), inelastic electron scattering in the solid, and the photoelectron-photohole interaction. For normal emission the streaking is determined by the normal component of the IR field. This allows restricting the TDSE to propagation in one dimension. The dynamical screening and penetration of the IR field (Supplementary Materials

Fig. S5) and the inelastic mean free path (MFP) (Supplementary Materials Fig. S6) are derived from ab-initio electronic structure calculations for WSe_2 (Supplementary Materials sections 2.2.3 and 2.2.4). For each atomic layer and initial state the streaking spectrogram is calculated separately and then added yielding the streaking spectrogram (Supplementary Materials Fig. S9) and the corresponding photoemission delays listed in Tab. 1. Note that this approach incorporates all previously demonstrated photoemission delay mechanisms that were identified based on various approaches (*11*, *12*, *15–23*): wave packet propagation (*24–27*), inelastic scattering in the bulk solid (*21*, *28*), initial states localization (*19*), and a realistic choice of the "streaking clock" position, i.e. the position along the photoelectron trajectory at which the electron starts to be exposed to the streaking field (*21*, *25*).

Compared to the experimental values the delays obtained using the 1D TDSE propagation alone (column labeled 1D TDSE in Tab. 1) are systematically too small by about a factor two. This discrepancy is robust with respect to realistic variations of the MFP (4 to 5 Å), the e-h interaction screening length, and of the exact position of the attosecond clock ($\pm$ 0.5 Å). Neither atomic delays nor propagation effects alone account for the experimentally observed delays. However, if propagation induced delays and atomic delays are joined the total delay (column "Theory Σ" in Tab. 1) matches the experimental observations. Based on this we conclude that the angular momentum of the initial localized atomic state affects the time-delay of photoelectrons in solids. Intra-atomic interactions substantially contribute to the total delay.

This observation is in contrast to state-of-the-art photoemission models that emphasize the translational invariance in the solid for initial and excited state. As demonstrated the initially excited localized wave packet is dominated by the spherical symmetry of the atom from which the electron is emitted. Only after some time, as the wave propagates to neighboring atoms, the

photoelectron feels the structure of the crystal. This complex evolution of a many-body system is not captured in common photoemission models and attosecond time-resolved photoemission spectroscopy thus provides access investigating this initial phase of the photoemission process in more detail. Incorporating this initial stage localized at the particular atom from which the electron is emitted is cornerstone of our model and any future models of solid state photoemission.

Fig. 1. Elementary steps in photoemission from the van der Waals crystal WSe₂. The WSe₂ substrate and the principle of attosecond time-resolved streaking spectroscopy are depicted. The surface held at room temperature is illuminated collinearly with a 300 as long EUV pulse with 91 eV center energy and an intense few-cycle IR streaking field (85° angle of incidence, p-polarized). The EUV pulses excite photoelectrons (here shown for the W 4f photoemission) that are then streaked in the IR field, i.e. are gaining or losing kinetic energy depending on the delay t_{IR}-t_{EUV} between EUV and IR pulse. As indicated in the upper left panel the initial stage of photoemission is dominated by intra-atomic processes: Within the Hartree-Slater (HS) approach the photoelectron wave (green) created by EUV excitation from the W 4f state (blue) is governed by the effective radial potential (red) composed of the HS potential U^{HS} and the centrifugal term. The wave packet propagation in the later stage is schematically depicted in the right panel. It is dominated by a one-dimensional (1D) potential that accounts for the inner potential U_{IP} of WSe₂ and the interaction with the remaining photohole. The inelastic mean free path (MFP) for the photoelectron is indicated as horizontal bar.

*Fig. 2. Attosecond time-resolved photoemission spectroscopy from WSe₂. (A) Long-term stability of the surface over 40 h. Background corrected photoemission spectra (Supplementary Materials Fig. S1A) recorded 30 min (black circles) and 40 h (red circles) after cleaving. The photoelectron peaks for VB, Se 4s, W 4f, and Se 3d are indicated.(**B**) Streaking spectrogram. As function of the delay between IR and EUV pulse the photoemission spectra (after background subtraction) are shown as density plot. For each delay the energy positions (overlaid symbols) of the VB, Se 4s, W 4f, and Se 3d emissions and the corresponding simultaneously fitted IR field*

time dependence (Supplementary Materials Eq. S1) yielding the delay parameters Δt for each

emission channel (continuous overlaid lines) are shown.

Fig.3. Relative photoemission delays. *The left part shows the relative photoemission delays*

$\Delta t_{\text{VB}-\text{Se 4s}}$, $\Delta t_{\text{Se 3d}-\text{Se 4s}}$, *and* $\Delta t_{\text{W4f}-\text{Se 4s}}$ *as function of time after cleaving for two different crystals*

indicated by different symbols (circles and squares) using the background subtraction method

based on a model spectrum (Supplementary Materials Fig. S1A). The horizontal error bars

indicate the time period in which the spectrogram was recorded and the vertical bars indicate

the uncertainty of the delay determination. In the right part the average delays obtained by

various background subtraction procedures are shown: background based on model spectrum

(red circle), parabolic background (black circle), combination of parabolic and Shirley

background with and without delay-dependent background (blue and green circle, respectively),

and delay-dependent background based on model spectrum (magenta circle).

X	$E_{kin}^{X} - E_{kin}^{\text{Se 4s}}$	Exp. $\Delta t_{X-\text{Se 4s}}$	Theory Σ total incl. HS / MCDF	Atomic delay HS / MCDF	Propagation del. 1D TDSE
VB 4p/5d	13.5 eV	12 ± 10	12 / 12	6 / 6	6
Se 3d	- 41.3 eV	28 ± 10	29 / 25	14 / 10	15
W 4f	- 19.3 eV	47 ± 14	44 / 36	20 / 12	24

Tab. 1. Comparison between experimental and theoretical photoemission delays in as. *The*

second column specifies the difference between the kinetic energies for X and Se 4s

photoelectrons. The third column summarizes the experimental delays as indicated in Fig. 3. The

4th column lists the summed intra-atomic and propagation induced delays derived using either

the HS or the MCDF approach (5th column) and 1D TDSE simulation of propagation in the solid

(6th column), respectively. For details see Supplementary Materials section 2.

References and Notes:

1. M. Schultze *et al.*, Delay in Photoemission. *Science*. **328**, 1658–1662 (2010).

2. K. Klünder *et al.*, Probing Single-Photon Ionization on the Attosecond Time Scale. *Phys. Rev. Lett.* **106**, 143002 (2011).

3. M. Ossiander *et al.*, Attosecond correlation dynamics. *Nat. Phys.* **13**, 280–285 (2016).

4. R. Pazourek, S. Nagele, J. Burgdörfer, Attosecond chronoscopy of photoemission. *Rev. Mod. Phys.* **87**, 765–802 (2015).

5. A. L. Cavalieri *et al.*, Attosecond spectroscopy in condensed matter. *Nature*. **449**, 1029–1032 (2007).

6. A. Klein *et al.*, Photovoltaic properties of WSe_2 single-crystals studied by photoelectron spectroscopy. *Sol. Energ. Mat. Sol. Cells*. **51**, 181–191 (1998).

7. F. Herman, S. Skillman, *Atomic Structure Calculations* (Prentice-Hall, 1963).

8. I. P. Grant, in *Methods in Computational Chemistry* (Plenum Press, New York, 1988), vol. 2, pp. 1–71.

9. M. Huppert, I. Jordan, D. Baykusheva, A. von Conta, H. J. Wörner, Attosecond Delays in Molecular Photoionization. *Phys. Rev. Lett.* **117**, 093001 (2016).

10. U. Fano, J. W. Cooper, Spectral Distribution of Atomic Oscillator Strengths. *Rev. Mod. Phys.* **40**, 441–507 (1968).

11. A. K. Kazansky, P. M. Echenique, One-Electron Model for the Electronic Response of Metal Surfaces to Subfemtosecond Photoexcitation. *Phys. Rev. Lett.* **102**, 177401 (2009).

12. A. G. Borisov, D. Sánchez-Portal, A. K. Kazansky, P. M. Echenique, Resonant and nonresonant processes in attosecond streaking from metals. *Phys. Rev. B*. **87**, 121110 (2013).

13. A. K. Kazansky, N. M. Kabachnik, Theoretical description of atomic photoionization by an attosecond XUV pulse in a strong laser field: effects of rescattering and orbital polarization. *J. Phys. B: At. Mol. Opt. Phys.* **40**, 2163–2177 (2007).

14. T. Finteis *et al.*, Occupied and unoccupied electronic band structure of WSe_2. *Phys. Rev. B*. **55**, 10400–10411 (1997).

15. C. Lemell, B. Solleder, K. Tőkési, J. Burgdörfer, Simulation of attosecond streaking of electrons emitted from a tungsten surface. *Phys. Rev. A*. **79**, 062901 (2009).

16. J. C. Baggesen, L. B. Madsen, Theory for time-resolved measurements of laser-induced electron emission from metal surfaces. *Phys. Rev. A*. **78**, 032903 (2008).

17. E. E. Krasovskii, Attosecond spectroscopy of solids: Streaking phase shift due to lattice scattering. *Phys. Rev. B*. **84**, 195106 (2011).

18. S. Nagele *et al.*, Time-resolved photoemission by attosecond streaking: extraction of time information. *J. Phys. B: At. Mol. Opt. Phys.* **44**, 081001 (2011).

19. C.-H. Zhang, U. Thumm, Effect of wave-function localization on the time delay in photoemission from surfaces. *Phys. Rev. A*. **84**, 065403 (2011).

20. C.-H. Zhang, U. Thumm, Probing dielectric-response effects with attosecond time-resolved streaked photoelectron spectroscopy of metal surfaces. *Phys. Rev. A*. **84**, 063403 (2011).

21. Q. Liao, U. Thumm, Initial-state, mean-free-path, and skin-depth dependence of attosecond time-resolved IR-streaked XUV photoemission from single-crystalline magnesium. *Phys. Rev. A*. **89**, 033849 (2014).

22. Q. Liao, U. Thumm, Attosecond Time-Resolved Photoelectron Dispersion and Photoemission Time Delays. *Phys. Rev. Lett.* **112**, 023602 (2014).

23. U. Heinzmann, in *Attosecond Physics*, L. Plaja, R. Torres, A. Zaïr, Eds. (Springer Berlin Heidelberg, Berlin, Heidelberg, 2013), *Springer Series in Optical Sciences*, pp. 231–253.

24. S. Neppl *et al.*, Attosecond Time-Resolved Photoemission from Core and Valence States of Magnesium. *Phys. Rev. Lett.* **109**, 087401 (2012).

25. S. Neppl *et al.*, Direct observation of electron propagation and dielectric screening on the atomic length scale. *Nature*. **517**, 342–346 (2015).

26. R. Locher *et al.*, Energy-dependent photoemission delays from noble metal surfaces by attosecond interferometry. *Optica*. **2**, 405 (2015).

27. Z. Tao *et al.*, Direct time-domain observation of attosecond final-state lifetimes in photoemission from solids. *Science*. **353**, 62–67 (2016).

28. I. Nagy, P. M. Echenique, Mean free path of a suddenly created fast electron moving in a degenerate electron gas. *Phys. Rev. B*. **85**, 115131 (2012).

29. S. Tougaard, Practical algorithm for background subtraction. *Surf. Sci.* **216**, 343–360 (1989).

30. E. L. Shirley, Theory and simulation of resonant inelastic X-ray scattering in s-p bonded systems: graphite, hexagonal boron nitride, diamond, and cubic boron nitride. *J. Elec. Spec.* **110**–**111**, 305–321 (2000).

31. F. Merschjohann *et al.*, in *Ultrafast Phenomena XIX*, K. Yamanouchi, S. Cundiff, R. de Vivie-Riedle, M. Kuwata-Gonokami, L. DiMauro, Eds. (Springer International Publishing, Cham, 2015), vol. 162 of *Springer Proceedings in Physics*, pp. 68–71.

32. F. Siek, thesis, Bielefeld University, Bielefeld (2016).

33. L. Eisenbud, thesis, Princeton University (1948).

34. E. P. Wigner, L. Eisenbud, Higher Angular Momenta and Long Range Interaction in Resonance Reactions. *Phys. Rev.* **72**, 29–41 (1947).

35. F. T. Smith, Lifetime Matrix in Collision Theory. *Phys. Rev.* **118**, 349–356 (1960).

36. F. A. Parpia, C. F. Fischer, I. P. Grant, GRASP92: A package for large-scale relativistic atomic structure calculations. *Comput. Phys. Commun.* **94**, 249–271 (1996).

37. S. Fritzsche, H. Aksela, C. Z. Dong, S. Heinäsmäki, J. E. Sienkiewicz, Theoretical Auger and photoionization studies for open-shell atoms and ions. *Nucl. Instrum. Methods B.* **205**, 93–98 (2003).

38. S. Fritzsche, Ratip – a toolbox for studying the properties of open-shell atoms and ions. *J. Elec. Spec.* **114**–**116**, 1155–1164 (2001).

39. S. Fritzsche, The Ratip program for relativistic calculations of atomic transition, ionization and recombination properties. *Comput. Phys. Commun.* **183**, 1525–1559 (2012).

40. U. Fano, Propensity rules: An analytical approach. *Phys. Rev. A.* **32**, 617–618 (1985).

41. E. E. Krasovskii, W. Schattke, Surface electronic structure with the linear methods of band theory. *Phys. Rev. B.* **56**, 12874–12883 (1997).

42. G. D. Mahan, Theory of Photoemission in Simple Metals. *Phys. Rev. B.* **2**, 4334–4350 (1970).

43. P. J. Feibelman, D. E. Eastman, Photoemission spectroscopy—Correspondence between quantum theory and experimental phenomenology. *Phys. Rev. B.* **10**, 4932–4947 (1974).

44. J. Javanainen, J. H. Eberly, Q. Su, Numerical simulations of multiphoton ionization and above-threshold electron spectra. *Phys. Rev. A.* **38**, 3430–3446 (1988).

45. E. Runge, E. K. U. Gross, Density-Functional Theory for Time-Dependent Systems. *Phys. Rev. Lett.* **52**, 997–1000 (1984).

46. R. Coehoorn, C. Haas, R. de Groot, Electronic structure of $MoSe_2$, MoS_2, and WSe_2. II. The nature of the optical band gaps. *Phys. Rev. B*. **35**, 6203–6206 (1987).

47. N. Troullier, J. L. Martins, Efficient pseudopotentials for plane-wave calculations. *Phys. Rev. B*. **43**, 1993–2006 (1991).

48. J. P. Perdew, A. Zunger, Self-interaction correction to density-functional approximations for many-electron systems. *Phys. Rev. B*. **23**, 5048–5079 (1981).

49. D. M. Ceperley, B. J. Alder, Ground State of the Electron Gas by a Stochastic Method. *Phys. Rev. Lett.* **45**, 566–569 (1980).

50. A. Zangwill, *Physics at surfaces* (Cambridge University Press, Cambridge, 1988).

51. L. Hedin, S. Lundqvist, in *Solid State Physics* (Elsevier, 1970), vol. 23, pp. 1–181.

52. P. M. Echenique, J. M. Pitarke, E. V. Chulkov, A. Rubio, Theory of inelastic lifetimes of low-energy electrons in metals. *Chem. Phys.* **251**, 1–35 (2000).

53. J. S. Dolado, V. M. Silkin, M. A. Cazalilla, A. Rubio, P. M. Echenique, Lifetimes and mean-free paths of hot electrons in the alkali metals. *Phys. Rev. B*. **64**, 195128 (2001).

54. B. L. Henke, E. M. Gullikson, J. C. Davis, X-Ray Interactions: Photoabsorption, Scattering, Transmission, and Reflection at E = 50-30,000 eV, Z = 1-92. *At. Data Nucl. Data Tables*. **54**, 181–342 (1993).

55. E. E. Krasovskii, W. Schattke, Calculation of the wave functions for semi-infinite crystals with linear methods of band theory. *Phys. Rev. B*. **59**, R15609–R15612 (1999).

56. V. Heine, On the General Theory of Surface States and Scattering of Electrons in Solids. *Proc. Phys. Soc.* **81**, 300–310 (1963).

57. O. Lang, Y. Tomm, R. Schlaf, C. Pettenkofer, W. Jaegermann, Single crystalline $GaSe/WSe_2$ heterointerfaces grown by van der Waals epitaxy. II. Junction characterization. *J. Appl. Phys.* **75**, 7814–7820 (1994).

58. R. Schlaf, O. Lang, C. Pettenkofer, W. Jaegermann, Band lineup of layered semiconductor heterointerfaces prepared by van der Waals epitaxy: Charge transfer correction term for the electron affinity rule. *J. Appl. Phys.* **85**, 2732–2753 (1999).

59. V. N. Strocov *et al.*, Three-dimensional band structure of layered $TiTe_2$: Photoemission final-state effects. *Phys. Rev. B*. **74**, 195125 (2006).

60. E. E. Krasovskii, K. Rossnagel, A. Fedorov, W. Schattke, L. Kipp, Determination of the Hole Lifetime from Photoemission: Ti 3d States in $TiTe_2$. *Phys. Rev. Lett.* **98**, 217604 (2007).

61. E. E. Krasovskii *et al.*, Photoemission from Al(100) and (111): Experiment and *ab initio* theory. *Phys. Rev. B*. **78**, 165406 (2008).

62. M. Frisch *et al.*, Gaussian 09, Revision E.01. *Gaussian 09, Revision E.01, Gaussian, Inc., Wallingford CT* (2010).

63. Y. Zhao, D. G. Truhlar, The M06 suite of density functionals for main group thermochemistry, thermochemical kinetics, noncovalent interactions, excited states, and transition elements: two new functionals and systematic testing of four M06-class functionals and 12 other functionals. *Theo. Chem. Acc.* **120**, 215–241 (2008).

64. G. G. Camiletti, S. F. Machado, F. E. Jorge, Gaussian basis set of double zeta quality for atoms K through Kr: Application in DFT calculations of molecular properties. *J. Comput. Chem.* **29**, 2434–2444 (2008).

65. A. Canal Neto, F. E. Jorge, All-electron double zeta basis sets for the most fifth-row atoms: Application in DFT spectroscopic constant calculations. *Chem. Phys. Lett.* **582**, 158–162 (2013).

66. M. Douglas, N. M. Kroll, Quantum electrodynamical corrections to the fine structure of helium. *Ann. Phys.* **82**, 89–155 (1974).

67. B. A. Hess, Applicability of the no-pair equation with free-particle projection operators to atomic and molecular structure calculations. *Phys. Rev. A*. **32**, 756–763 (1985).

68. B. A. Hess, Relativistic electronic-structure calculations employing a two-component no-pair formalism with external-field projection operators. *Phys. Rev. A*. **33**, 3742–3748 (1986).

69. G. Jansen, B. A. Hess, Revision of the Douglas-Kroll transformation. *Phys. Rev. A*. **39**, 6016–6017 (1989).

70. M. Torrent-Sucarrat, P. Salvador, P. Geerlings, M. Solà, On the quality of the hardness kernel and the Fukui function to evaluate the global hardness. *J. Comput. Chem.* **28**, 574–583 (2007).

71. M. Torrent-Sucarrat, P. Salvador, M. Solà, P. Geerlings, The hardness kernel as the basis for global and local reactivity indices. *J. Comput. Chem.* **29**, 1064–1072 (2008).

72. M. D. Feit, J. A. Fleck, A. Steiger, Solution of the Schrödinger equation by a spectral method. *J. Comput. Phys.* **47**, 412–433 (1982).

Any Additional Author notes: F.S. and S.N. performed the experiments. F.S., S.N., P.B., M.H., C.S., and N.M. contributed to the development and operation of the experimental setup and Se.F. provided the WSe_2 crystals and supervised in-situ preparation. F.S., S.N., and W.P. analyzed the experimental results. A.K.K. developed the 1D TDSE propagation model and coordinated the various theoretical activities concerned with intra-atomic delays (A.K.K., St.F., and N.M.K.), electron MFP in WSe_2 and the dynamically IR streaking field distribution at the WSe_2-vacuum interface (V.M.S. and R.D.M.), effective mass of photoelectrons in WSe_2 (E.E.K.), and the projected initial states (M.T. S.). P.M.E., U.H., and W.P. supervised the project.
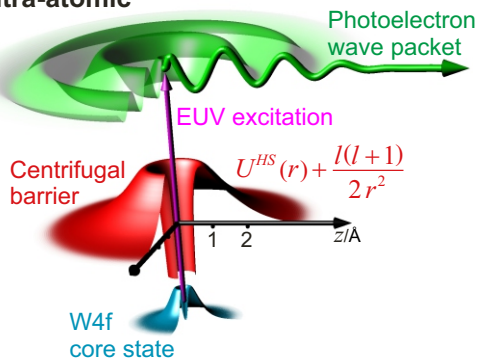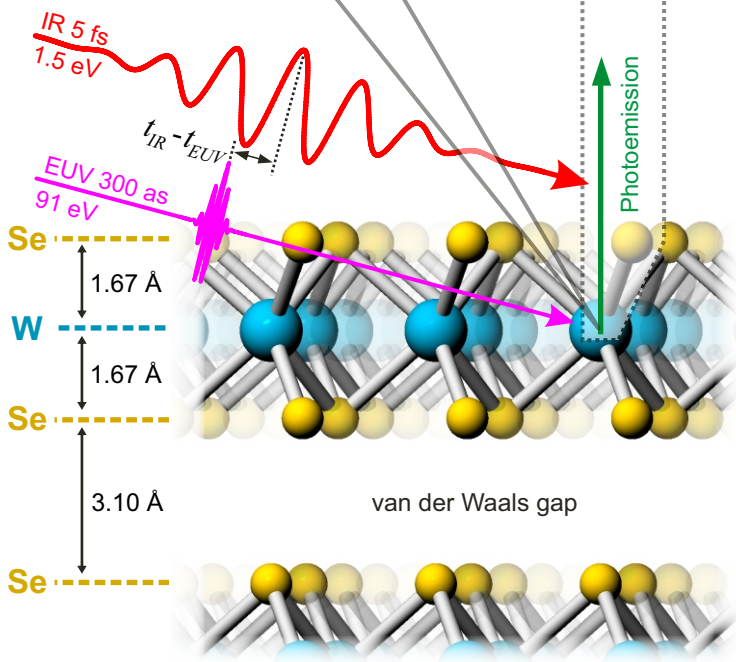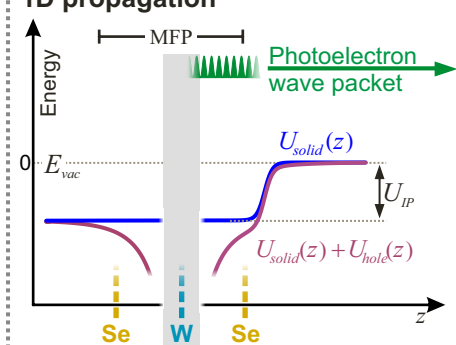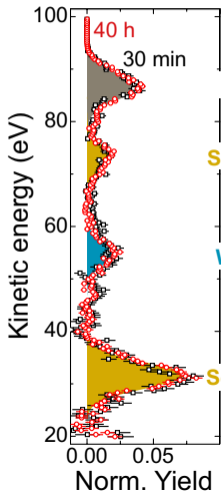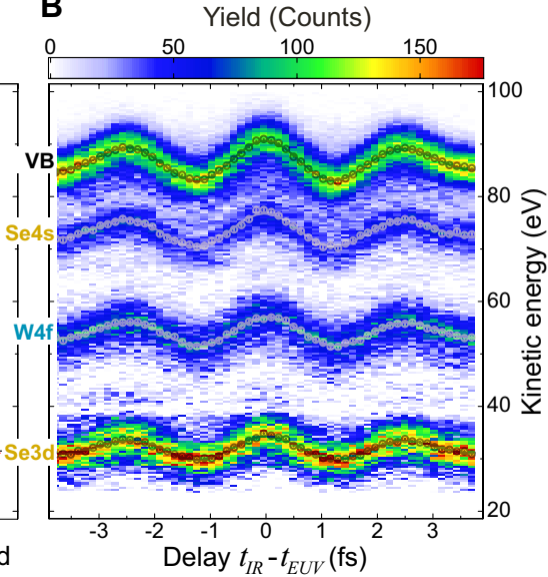
Supplementary Materials:

Methods

Figures S1-S9

References (29-72)

Intra-atomic

Photoelectron wave packet

EUV excitation

Centrifugal barrier

$$U^{HS}(r) + \frac{l(l+1)}{2r^2}$$

W4f core state

$z/\text{Å}$

1D propagation

MFP

Photoelectron wave packet

Energy

E_{vac}

0

$U_{solid}(z)$

U_{IP}

$U_{solid}(z) + U_{hole}(z)$

Se   W   Se

z

IR 5 fs
1.5 eV

$t_{IR} - t_{EUV}$

EUV 300 as
91 eV

Photoemission

Se

1.67 Å

W

1.67 Å

Se

3.10 Å

van der Waals gap

Se

A

Kinetic energy (eV)

40 h
30 min

VB
Se4s
W4f
Se3d

Norm. Yield

B Yield (Counts)

0   50   100   150

Kinetic energy (eV)

Delay $t_{IR} - t_{EUV}$ (fs)

Materials and Methods – Contents

Materials and Methods

In the Supplementary Materials we provide further details on the used method of attosecond time-resolved streaking spectroscopy and the related data evaluation procedure in section 1. The theoretical model used in the analysis of the experimental data, is described in section 2. In Subsection 2.1 we consider the intra-atomic delays accumulated in the very initial stage of the photoemission process, i.e. well within the atom from which the photoelectron is emitted. In Section 2.2 we present the general description of propagation of the wave packet of an electron, ejected by an EUV pulse from an atom inside the bulk. Here we introduce the quantities relevant for description of the electron propagation in the solid. Section 3 summarizes experimentally and theoretically derived relative photoemission delays.

1 Attosecond time-resolved streaking spectroscopy

The attosecond streaking experiments were performed under ultra-high vacuum (UHV) conditions (base pressure $< 10^{-10}$ mbar) in an experimental chamber that had already been used for streaking spectroscopy in an equivalent setup (5). WSe$_2$ crystals were cleaved under UHV conditions (10^{-10} mbar) and EUV photoemission spectra and streaking spectrograms were recorded at room temperature over periods of up to 3 days without sign of degradation (Fig. 2a).

A commercial femtosecond laser system (Femtopower PRO) provided intense carrier envelope phase (CEP) stabilized fs-pulses (30 fs pulse duration, 800 nm center wavelength) at a repetition rate of 1 kHz. Self-phase modulation in a Neon-filled hollow core fiber (3.1 bar, 250 μm inner diameter, 1 m length) produced an octave spanning spectrum and 5-6 fs long few-cycle pulses after a chirped mirror compressor. Single attosecond EUV pulses were created via high harmonic generation (HHG) in a Neon gas target, suppression of the low order high harmonics using a 150 nm thick Zirconium absorber, spectrally filtering the cut-off region of the HHG spectrum using a multilayer EUV focusing mirror with a spectral bandwidth of 6 eV and a peak reflectance at 91 eV, and adjusting the CEP of the IR pulse to a cosine pulse. For this CEP the maximum of the IR pulse envelope coincides with a maximum of the carrier frequency oscillation. As a result the highest EUV radiation energy in the cut-off regime of the HHG spectrum is generated only once during a single IR pulse and spectral filtering of this highest energy part of the spectrum delivers isolated single attosecond EUV pulses. The smaller divergence of the EUV radiation compared to the IR beam used for HHG was employed for separating both spectral components for time-resolved spectroscopy using a coaxial mirror assembly. The diameter of Zr absorber and EUV multilayer mirror match the diameter of the EUV radiation in the beam and since the IR radiation is absorbed by the Zr layer the inner part of the beam contained just EUV radiation. The outer part of the beam containing only IR radiation was directed onto the sample surface by the outer mirror of the coaxial assembly. Alignment of the inner EUV mirror and outer IR mirror guaranteed spatial and temporal overlap of IR and EUV pulse on the sample surface. Axial displacement of the EUV mirror using a stabilized translation stage allowed controlling the temporal delay $t_{IR} - t_{EUV}$ between IR and EUV pulse. The IR intensity on the sample surface was adjusted using an iris aperture in the beam.

EUV and IR pulses impinge on the surface under an angle of incidence of 85°. The created photoelectrons emitted in normal emission were detected using a field-free time-of-flight electron spectrometer. Gas phase photoemission from Xe was used to calibrate the spectrometer. Before and after the recording of streaking spectrograms reference EUV photoemission spectra were recorded to guarantee that the experimental conditions remained stable.

1.1 Inelastic background subtraction and error analysis

The analysis of a solid state photoemission spectrum requires an assessment of the various spectral components and the inelastic background. Fig. S1A shows a WSe_2 EUV photoemission spectrum. The large bandwidth of the EUV excitation pulse broadens the spectral features and for example the spin-orbit splitting of the Se 3d and W4f core levels are no longer resolved. In addition, an Auger peak related to the recombination of a VB electron with a photohole in the Se 3d core level further impedes the decomposition of the spectrum. The measured spectrum can be well fitted using a model spectrum that is based on a series of distinct photoemission components (color shaded peaks in Fig. S1A) convoluted with the excitation spectrum, their inelastic background signals also convoluted with the excitation spectrum, the Auger peak, its inelastic background, and a contribution of secondary electrons for kinetic energies smaller than about 30 eV (not indicated in Fig. S1A). Note that the latter three components are not affected by the bandwidth of the excitation pulse.

The Tougaard approach (*29*) is used to model the inelastic background for each photoemission component and the Auger peak (color shaded peaks in Fig. S1A) and then convoluted with the excitation spectrum. Lower and upper energy edge of the Auger peak are determined by the VB spread over about 6-7 eV (*14*) and the Se 3d core level energy. This restricts possible models for the background function. After subtraction of the inelastic background and the Auger peak the four different photoemission components are clearly visible (lower panel of Fig. S1A). Note that the Se 3d peak now appears broader and matches the bandwidth expected from the convolution of the spin-orbit split Se 3d peaks and the EUV excitation spectrum.

Although the just introduced model spectrum reproduces the measured spectrum rather well it is not unambiguously defined. Another choice of the background function affects the peak positions and therefore might significantly alter the small delays measured in attosecond streaking spectroscopy. Note that for example the inelastic contribution underneath the elastic photoemission peak might streak with the same delay as the elastic peak, a different delay, or might even be completely unaffected by the IR streaking field. To test the robustness of the determined delays with respect to this ambiguity five different background subtraction procedures based on three different background functions were implemented. The corresponding three background functions are shown in Fig. S1B. In addition to the already introduced model function (red dashed line) a purely parabolic background function (black dashed line) and a combination of a parabolic background combined with a Shirley background (*30*) for the Se 4s and VB photoemission peaks (solid blue line) are employed. Note that the subtracted background varies substantially between the three methods. In addition the subtraction of a parabolic background for the Se 3d peak leads to unphysically narrow Se 3d peaks and hence the

corresponding streaking delays were omitted. However, as discussed in the main text the evaluated delays are robust with respect to these significantly varying background subtraction methods and the correspondingly determined relative delays scatter only within their statistical uncertainty.
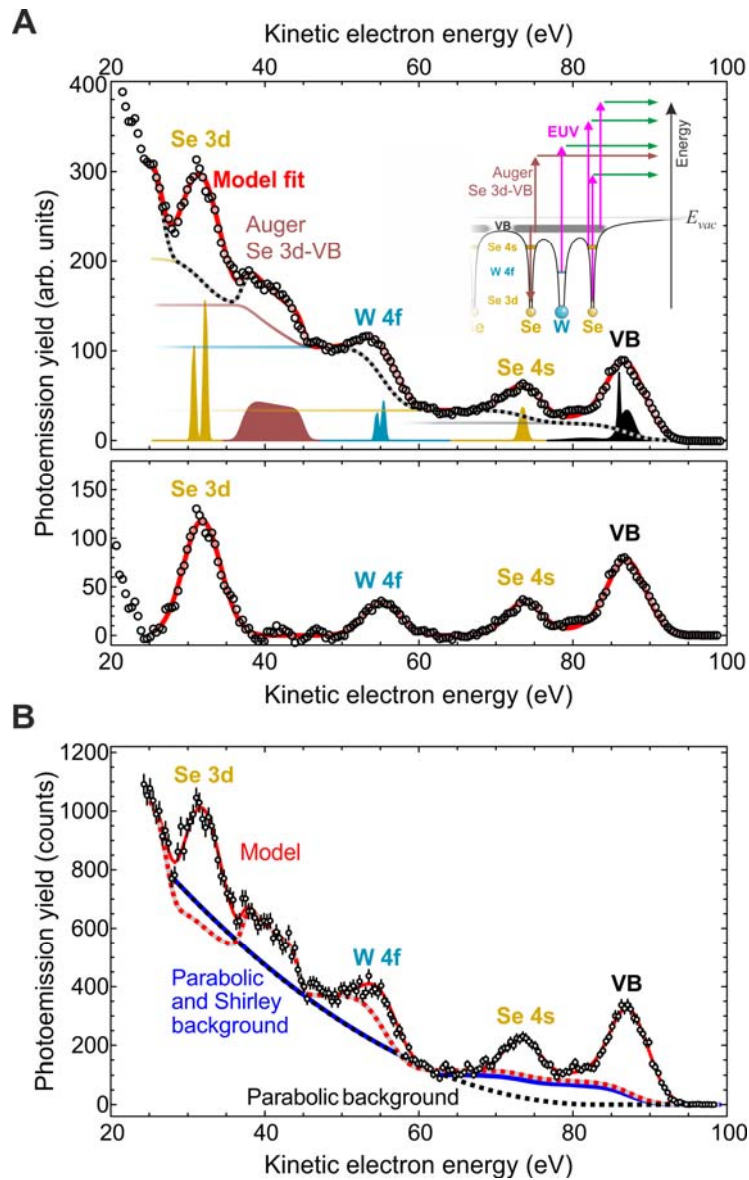
Fig. S1. Decomposition of the EUV photoemission spectrum and inelastic background subtraction. *(A) WSe$_2$ EUV photoemission spectra for photoexcitation with 300 as EUV pulses with 91 eV center photon energy (open circles) without and with background subtracted are shown in the upper and lower panel, respectively. The shaded peaks in the upper panel represent the different photoemission components prior to convolution with the EUV excitation spectrum and the Auger peak related to the recombination of a valence band electron with a hole in the Se*

*3d core level. The correspondingly colored lines indicate the inelastic background for these spectral components. The total inelastic background is shown as black dashed line. A schematic excitation scheme appears as inset in the upper panel. The lower panel shows the photoemission spectrum and model spectrum (red line) after background subtraction.(**B**) Comparison of background subtraction procedures. For an EUV photoemission spectrum (black circles) the background contributions are shown for a parabolic shaped background (dashed black line), a combination of parabolic and Shirley-type background for VB and Se4s emission (blue line), and the model background determined as in **A** (red dashed line).*

To reflect the uncertainties arising from ambiguous background subtraction methods the averaged relative photoemission delays noted in the right part of Fig. 3 and tabulated in Tab. 1 are calculated as arithmetic mean of the delays determined for the different background subtraction methods. Note that also the standard deviation of the delays is determined as arithmetic mean since the delays determined by different evaluation methods are correlated.

In addition, sources for systematic errors were minimized. In a preliminary study of the same material we reported different relative delays (*31*), a discrepancy that was recently identified as arising from a spurious magnetic field in the setup (*32*). The impact of an observed susceptibility of photoemission delay differences on magnetic fields in the order of up to 0.5 as μT^{-1} was minimized by applying field compensation, magnetic shielding, and nonmagnetic materials resulting in residual magnetic fields < 1 μT. The comparison of measured streaking spectrograms and spectrograms simulated for different linear chirp of the EUV pulse limits its actual value to < 0.01 fs^2 and the related systematic uncertainty of the delay differences to < 2 as.

1.2 Analysis of streaking spectrograms

After applying the various background subtraction procedures to each individual spectrum of a streaking spectrogram the peak positions of the four different spectral components were deduced by simultaneously fitting four Gaussians. Cases in which the spectral linewidth obtained in this fit is smaller than the energetic bandwidth of the EUV spectrum because of an unphysical background subtraction were omitted from further analysis. After conversion of the obtained kinetic energies to linear momenta the photoemission delays Δt were determined by least-square fits of the streaking curves using

$$S(\tau) = S_0 \, e^{-4\ln2((\tau+\Delta t)/t_L)^2} \sin\left(\omega_L(\tau+\Delta t) + GVD(\tau+\Delta t)^2 + \varphi_{CE}\right) + S_{offset} \tag{S1}$$

as fit function, where $\tau = t_{IR} - t_{EUV}$ is the delay between IR and EUV pulse, S_0 and S_{offset} are amplitude and offset of the streaking curve, respectively, t_L the duration of the IR Pulse, ω_L the center frequency of the IR pulse, GVD allows for linear chirp of the IR pulse, and φ_{CE} is the carrier envelope phase. The parameters determined by the IR field (t_L, ω_L, GVD, φ_{CE}) were chosen identical for the four different streaking curves derived from an individual streaking

spectrogram. In contrast to gas phase streaking, S_0 could vary slightly for different emission channels because the IR field is no longer homogeneous and IR field penetration into the material occurs.

1.3   Data averaging

The determined relative photoemission delays rely both on streaking measurements with good statistics and on an averaging over different measurements. Note that the averaging over individual measurements does not serve primarily to decrease the experimental uncertainty since similar uncertainties are also reached in individual measurements. The averaging serves to exclude effects due to sample and surface variability as well as possible surface contamination and other degradation processes such as laser damage.

The streaking measurements were performed using two different WSe$_2$ crystals and on different positions on each crystal. Neither aspect significantly influenced the obtained average relative delays. We performed these averages independently for both surfaces and obtained within the experimental uncertainty identical relative delays. Based on this we decided that we can average over the whole ensemble of streaking delay measurements. In order to make this procedure transparent we show the corresponding average delays in Tab. S1. Note that in all cases discussed here the resulting average delays reflect also the uncertainty inflicted by the different data evaluation procedures as they are discussed in Supplementary Materials section 1.1.

Tab. S1. Average relative delays determined independently for the different WSe$_2$ crystals

	$\Delta t_{\text{VB-Se4s}}$ [as]	$\Delta t_{\text{W4f-Se4s}}$ [as]	$\Delta t_{\text{Se3d-Se4s}}$ [as]
Sample 1	8± 11	49±15	30±13
Sample 2	15±8	43±12	28±9
Average	**12±10**	**47±14**	**28±10**

Besides sample variability surface degradation is another big concern. Even the slightest change of the surface conditions can significantly alter the observed photoemission delays. Actually the choice of the van der Waals material WSe$_2$ is a big advantage in this respect since the cleaved surface is rather inert. Still, adsorbates might lead to a drift of the measured delays, and could influence the obtained average delays. In the analysis of the measurements we took care to identify possible surface modifications: Between each streaking measurement EUV photoemission spectra with no IR light present were recorded to check for possible spectrum modifications. Both, modifications in the spectrum and variations in the total yield would

indicate surface contamination or degradation. For all shown experimental results no such evidence for a possible surface modification was observed.

However, there might still have occurred undetected modifications influencing the streaking measurements as function of time after cleavage. This effect could be analyzed by averaging the delays over sub-ensembles of the whole data set. To illustrate the possible impact of evaluating such sub-ensembles we draw the attention to an effect in the data set that might reflect such a possible trend in the measurements: The delays recorded for the largest period after cleaving (about 32 and 35 h after cleaving) appear all close to the lower border of the band marking the error margins (Fig. 3). Based on this one might suspect that some surface changes affect the streaking measurement and systematically reduces the delays. Tab. S2 summarizes the average delays for the full data set and a data set in which the last two measurements were omitted. The average delays for both sets of data again agree within the statistical uncertainty. Note that the omission of the last two data points even reduces the error margins of the delays and provides clearer evidence of the reported photoemission sequence ordered according to the initial state angular momentum s,p,d, and f. However, omission of the last two data points cannot be rationalized and we therefore report averages over the whole data set.

Tab. S2. Average relative delays for a sub-ensemble of the data set shown in Fig. 3

	$\Delta t_{\text{VB-Se4s}}$ [as]	$\Delta t_{\text{W4f-Se4s}}$ [as]	$\Delta t_{\text{Se3d-Se4s}}$ [as]
All data points in Fig. 3	12± 10	47±14	28±10
Omitting last two data points in Fig. 3	17±8	50±13	28±10

Summarizing, we found no significant deviation of the average delays in any of our tests analyzing sub-ensembles of the whole data set. Accordingly we take averages over all measurements of both crystals, all times after cleaving and varying sample positions. The resulting reported error margins reflect the impact of unavoidable variability and statistical uncertainty, both in the measurement and in the delay evaluation procedure.

2 Quantum mechanical model for solid state photoemission delays

In the following the basic principles of the methods used to theoretically determine photoemission delays are outlined. The theoretically determined photoemission delays rely on separate treatment of the intra-atomic delay (Section 2.1) and the delay arising from propagation effects in the solid (Section 2.2). The separation in two contributions is based on the following consideration: Atomic photoemission delays in many-electron atoms are determined by intra-atomic effects and the Coulomb phase accumulated for larger separations. The Coulomb phase induced delay is known (*4*) and thus the delay accumulated outside the atom can be subtracted from the total delay determined from atomic photoemission theory. After subtraction of the Coulomb delay the derived atomic delays only reflect the intra-atomic effects occurring in the very initial stage of the photoemission process. In addition the relative delays accumulated in the bulk-like propagation in this initial phase of the photoemission process are negligible and hence both contributions can be treated independently. Tests based on the WKB approximation confirmed the separability of both contributions.

2.1 Intra-atomic photoemission delays

The intra-atomic delay in photoemission is related to the Eisenbud–Wigner–Smith (EWS) delay. In the seminal papers (*33–35*) the time delay τ_{sc}^{EWS} for a wave packet scattering by a potential was related to the scattering phase-shift $\delta(E)$ for the center kinetic energy E of the wave packet by $\tau_{sc}^{EWS} = 2d\ \delta(E)/\mathrm{d}E$. Half of this delay reveals itself in photoionization of atoms as well (*4*). We keep the notation EWS delay when consider the delay in photoemission.

The photoionization process may be thought as consisting of the two stages: primary excitation of the electron and then propagation of the excited electron in the field of the core. One can compare an atom-ionization process in the case of a solitary atom and in the case of an atom embedded in the solid. From the physical point of view, the main difference is the substitution of the Coulomb field of the core by the corresponding screened Yukawa field. Since the Yukawa field (Eq. S15) is taken into account with the TDSE wave packet propagation we extract this atomic delay by subtracting the Coulomb delay. Note that in computation of the atomic delays for an atom inside the bulk the kinetic energy E_{bulk} of the ejected electron has to be taken relative to the mean potential in the bulk, i.e. $E_{bulk} = E - U_{IP}$, where E is the kinetic energy of the emitted electrons in vacuum and U_{IP} is the inner potential of WSe$_2$. The atomic delays (5th column in Tab. 1) were derived using, both, an single-configuration Hartree-Slater (HS) model (*7*) and the Multiconfiguration Dirac-Fock (MCDF) approach (*8*) which takes into account electron correlations and relativistic effects.

2.1.1 Single-configuration Hartree-Slater method

In the single-configuration approximation the initial (ground) state is presented as a Slater determinant based on the single-electron wave functions. The latter are calculated within the Hartree-Slater approximation. The final state with one electron in continuum is considered within the frozen core approximation. The continuum wave function $\psi(\mathbf{r})$ of the emitted electron is calculated using the Hartree-Slater potential $U^{HS}(r)$ derived via method developed by Herman and Skillman (*7*) which is widely used in description of atomic inner-shell phenomena.

The large-*r* asymptote of the wave function of an electron emitted from an initial state with angular momentum l_0 of a single isolated atom by monochromatic electromagnetic field reads:

$$
\psi(r,\theta,\phi) \cong \frac{\exp\left(i\left(kr + \ln(2kr)/k\right)\right)}{r}
$$
$$
\times \sum_l \left[Y_{l0}(\theta,\phi) \langle l,0|n_z|l_0,0\rangle \exp\left(-i\left(\frac{l\pi}{2} + \sigma_l(k) + \delta_l^C(k)\right)\right) R_{lk} \right],
$$
(S2)

where $l = l_0 \pm 1$ and $R_{lk} = \int_0^\infty P_{l,k}(r)\frac{\mathrm{d}}{\mathrm{d}r}\Phi_0(r)\mathrm{d}r$. Here $P_{l,k}(r)$ is the radial part of the wave function of the final continuum state with the small-*r* asymptote proportional to r^{l+1} and large-*r* asymptote given by

$$
P_{lk}(r) \cong B \sin\left(kr + \ln(2kr)/k - \frac{l\pi}{2} + \sigma_l(k) + \delta_l^C(k)\right),
$$
(S3)

where k is the momentum of the ejected electron, $\delta_l^C(k) = \arg\left(\Gamma\left(1 + l - i/k\right)\right)$ is the conventional Coulomb phase-shift for the electron with angular momentum l, $\sigma_l(k)$ is the intrinsic phase-shift due to a short range part of the potential of the positive ion, and B is the amplitude of the radial wave function.

In our problem we consider the electrons ejected along the external field, i.e. $\theta = \phi = 0$. Also, in propagation of the wave packet in bulk, instead of Coulomb field, we have used the screened Yukawa potential since the Coulomb field of an ion is quickly screened in the bulk. Therefore, in the present case, one has to omit the Coulomb contribution δ_l^C from the total phase. The wave function of the ejected electron asymptotically along *z*-direction is then given by

$$
\psi(z) \cong \sum_l \left[Y_{l0}(0,0) \langle l,0|n_z|l_0,0\rangle \exp\left(-i\left(kz - \frac{l\pi}{2} + \sigma_l(k)\right)\right) R_{lk} \right]
$$
$$
= \exp(ikz) A_{eff}(k) \exp\left(i\delta_{eff}(k)\right),
$$
(S4)

where $Y_{l0}(0,0) = \sqrt{(2l+1)/4\pi}$ and $\langle l-1,0|n_z|l,0\rangle = l/\sqrt{4l^2 - 1}$. Equation S4 is a definition of new quantities, $A_{eff}(k)$ and $\delta_{eff}(k)$. This accounts for the fact that the electron waves with

various angular momenta but the same energy must be added coherently, if the electron emission at a given solid angle is considered.
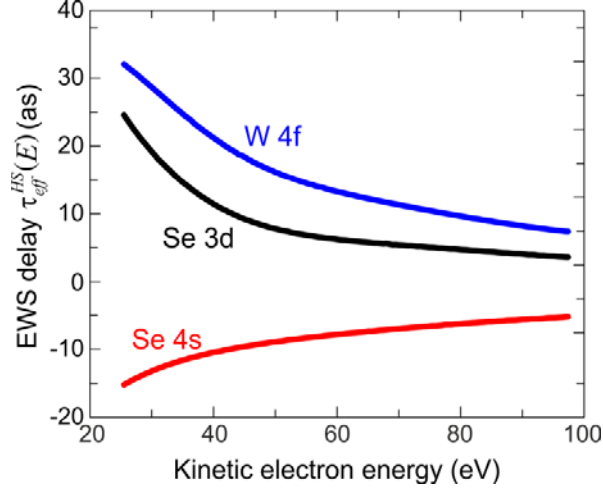

Fig. S2. Intra-atomic EWS photoemission delay $\tau_{\mathit{eff}}^{\mathit{HS}}$ **in HS approximation.** *EWS photoemission delay* $\tau_{\mathit{eff}}^{\mathit{HS}}$ *calculated based on Eq. S8 as function of the photoelectron kinetic energy for the different emission channels for Se 4s (red), Se3d (black), and W 4f (blue).*

In the calculations presented here, the single-electron radial matrix elements R_{lk} and partial phases $\sigma_l(k)$ were calculated using the Hartree-Slater potential $U^{HS}(r)$ (7). In the considered case, the short ionizing EUV pulse is quite broad in energy and the outgoing electron wave packet is

$$W(z,t) = \int_0^\infty \exp\left[i\left(kz - \frac{k^2 t}{2}\right)\right] A_{\mathit{eff}}(k) \exp\left(i\,\delta_{\mathit{eff}}(k)\right) \tilde{\mathcal{E}}_{EUV}\left(\frac{k^2}{2} - E\right) \mathrm{d}k. \tag{S5}$$

Here $\tilde{\mathcal{E}}_{EUV}(\omega)$ is the Fourier transform of the EUV pulse envelope, $E = \varepsilon_0 + \omega_{EUV}$ is the center kinetic energy of the photoionized electron. The large-z and large-t asymptote of the wave packet is determined by the stationary point

$$z - k\,t + \frac{\mathrm{d}\delta_{\mathit{eff}}(k)}{\mathrm{d}k} = 0, \tag{S6}$$

indicating that the wave packet arrives with a delay

$$t = \frac{z}{k} - \frac{1}{k}\frac{\mathrm{d}\delta_{\mathit{eff}}(k)}{\mathrm{d}k} = \frac{z}{k} - \tau^{EWS}(E). \tag{S7}$$

Thus in our case the conventional EWS delay

$$\tau_{\mathit{eff}}^{HS}(E) = \frac{\mathrm{d}\delta_{\mathit{eff}}(E)}{\mathrm{d}E} \tag{S8}$$

is determined by the effective phase-shift which includes the contributions from both available angular momenta coherently.

2.1.2 Multi-configuration Dirac-Fock approximation

In the relativistic multi-configuration Dirac-Fock (MCDF) approach, which takes into account electron-electron correlations and relativistic effects (*8, 36, 37*), both the initial atomic and the final ionic wave functions are approximated as linear combinations of configuration state functions (CSFs) of the same overall symmetry

$$|\alpha, \pi J\rangle = \sum_{r=1}^{n_c} c_r(\alpha) |\xi_r, \pi J\rangle, \tag{S9}$$

where πJ are the parity and the total angular momentum of the atomic system. The CSFs $|\xi_r, \pi J\rangle$ are constructed as anti-symmetrized products of a common set of orthonormal orbitals. These orbitals are optimized self-consistently on the basis of the Dirac-Coulomb Hamiltonian. In this work the MCDF atomic and ionic wave functions as well as complex photoionization amplitudes have been obtained using computer packages GRASP 14 (*36, 37*) and RATIP (*38, 39*). The continuum wave functions, necessary for computation of the dipole amplitudes, have been calculated in the state-dependent potential with exchange. The computed photoionization amplitudes and phases for each particular channel have been used for calculating the time-delay with the help of Eq. S4 and Eq. S8.

Note that in the MCDF approach a large number of many-body configurations i in the remaining ion contribute to one photoemission channel j $(j = \text{VB}, \text{Se } 4s, \text{W } 4f, \text{Se } 3d)$. The calculated final ionic states have in general slightly different energies and for a single-EUV-photon absorption process each individual ion remains in one particular configuration. Therefore the corresponding configurations i of the ejected electron and ion have to be added incoherently. The total photoionization cross section is the sum of partial cross sections while the photoelectron phases in different channels are different. The electron EWS delay must be computed as the mean value of the EWS delays $\tau_{eff}^i(k)$ (*4*) using

$$\tau_{eff}^{MCDF}(k) = \frac{\sum_i \sigma^i \tau_{eff}^i(k)}{\sum_i \sigma^i}, \tag{S10}$$

where σ^i is the partial cross section for a particular many-body configuration i, and $\tau_{eff}^i(k)$ is the electron delay for configuration i defined by Eq. S4 and Eq. S8.

2.1.3 Interpretation of intra-atomic delays

An intuitive interpretation of the intra-atomic delays may be provided in the framework of the Hartree-Slater method. The electron-electron interaction within the atom effectively screens

the Coulomb interaction with the nucleus resulting in the spherically symmetric self-consistent attractive potential, which is approximately represented by the Hartree-Slater potential U^{HS}. The full effective potential $U_{eff}^{HS}(r)$ acting on an electron with the angular momentum l within the atom is the sum of this attractive potential and the repulsive centrifugal term proportional to $l(l+1)/r^2$ (Fig. S3 and Fig. 1). According to the dipole transition selection rule $\Delta l = \pm 1$ two partial waves l_{i-1} and l_{i+1} coherently contribute to atomic photoionization from the l_i subshell. However, it is well known that in general the l_{i+1} contribution is dominant (40). Thus to a good approximation the initial orbital angular momentum of the electron fixes its final one. For high enough final angular momentum ($l \geq 2$) the effective potential may have a complicated profile (see examples in Fig. 1 of the main manuscript and in Fig. S3). The shape of the l-dependent effective potential strongly depends on the atomic number Z reflecting periodic atomic structure (10). Within the semiclassical approximation, in which the link between the time delay and the phase shift is straightforward, the time delay is the difference between the times of flight of a particle with given energy, starting from the corresponding turning points in the effective potential and in the centrifugal potential only, until some large distance. Obviously, the time delay depends on l and therefore on the orbital angular momentum of the initial state. Particular value of the time delay of the outgoing electron is determined by the peculiarities of the effective potential. Thus, the impact of the centrifugal barrier varies with electron energy and atomic number Z, increasing with increase of l. Because of the r^{-2} radial dependence of the centrifugal term in the effective potential the impact of the centrifugal barrier is most pronounced for radial distances below ~1 Å and thus the corresponding delay is accumulated in the very initial stage of the photoemission process.
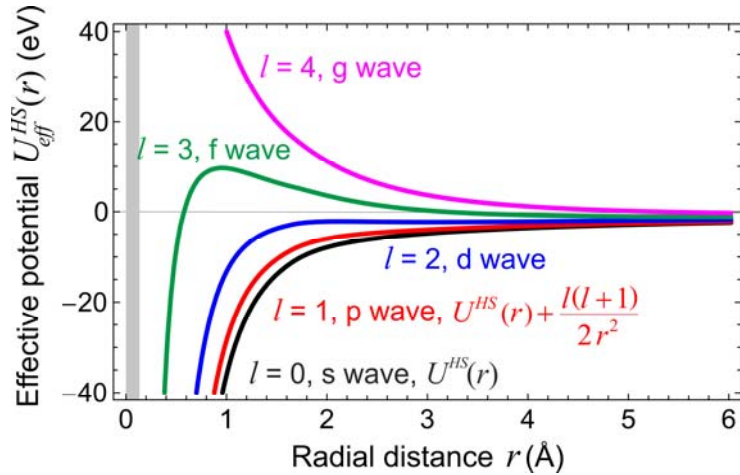

Fig. S3. Effective potential $U_{eff}^{HS}(r)$ for W. *Based on the corresponding Hartree-Slater potential U^{HS} the effective potential $U_{eff}^{HS}(r)$ is shown for different angular momenta l=1,2,3, and 4. The gray shaded area for small r indicates that the inner repulsive part of $U_{eff}^{HS}(r)$ is not shown in this range of r for clarity reasons.*

Note that this intuitive picture provides just a qualitative explanation of the effect. The actual energy dependent phases and thus also the related photoemission delays depend critically on details of the effective potentials and can only be determined from full quantum mechanical calculations as they were used to determine the atomic delays in this study (see Supplementary Materials section 2.1.1 and 2.1.2). This treatment then accounts for the effects of transition matrix elements and all subtleties of the effective potential.

2.2 Photoemission delays due to propagation in the solid

For modelling the photoelectron propagation in the bulk and outside the solid we rely on a single-particle time-dependent Schrödinger equation approach (TDSE). The photoemission process can then be described with the TDSE equation (atomic units are used in all equations below):

$$
i\frac{\partial}{\partial t}\Psi(\mathbf{r},t) = -\frac{1}{2}\Delta\Psi(\mathbf{r},t) + \left(U_{solid}(\mathbf{r}) + U_{hole}(\mathbf{r}) - iU_{\Gamma}(\mathbf{r}) - E\right)\Psi(\mathbf{r},t)
$$
$$
+ \left(iA_{EUV}(t)\frac{\partial}{\partial z} + \mathcal{E}_{IR}(t)U_{IR}(z)\right)\Psi(\mathbf{r},t)
\tag{S11}
$$

with initial condition $\Psi(\mathbf{r},t) = \exp(-i\varepsilon_0 t)\Phi_0(\mathbf{r})$ for $t \to -\infty$. Here ε_0 is the energy of the initial state from which electron is ejected due to absorption of an EUV photon, $\Phi_0(\mathbf{r})$ is the initial wave function, and $A_{EUV}(t) = A_0(t)\cos(\omega_{EUV}t)$ is the vector potential of the EUV field where the vector potential envelope $A_0(t)$ is chosen as Gaussian and the carrier frequency of the EUV pulse ω_{EUV} is not important within the approximation used here. $\mathcal{E}_{IR}(t)$ and $U_{IR}(z)$ are the temporal evolution and spatial profile of the potential of the IR laser pulse, respectively.

The method originally developed for gas phase streaking (13) is adapted here to reflect the dominant effects in solid state streaking. For normal emission the streaking effect is dominated by the normal component of the IR field chosen here as z-component and the TDSE is treated using a one-dimensional potential. Based on the assumption that the initial state $\Phi_0(z)$ remains unaffected by the EUV excitation, i.e. the EUV pulse excites only a very minor fraction of the initial state population, and the rotating wave approximation the total wave function $\Psi(z,t)$ can be written as

$$
\Psi(z,t) = e^{-i\omega_0 t}\Phi_0(z) + e^{-i\omega t}\Phi(z,t),
\tag{S12}
$$

where $\Phi(z,t)$ is the photoemission wave function. $\hbar\omega = \hbar\omega_0 + \hbar\omega_{EUV}$ is the center kinetic energy of the emitted photoelectrons if no streaking occurs, with the initial state energy $\hbar\omega_0$ and the center EUV pulse photon energy $\hbar\omega_{EUV}$. Based on Eq. S12 the equation of motion for the photoemission wave function $\Phi(z,t)$ is obtained as

$$i\hbar \frac{\partial}{\partial t}\Phi(z,t) = -\frac{\hbar^2}{2m_e}\frac{\partial^2}{\partial z^2}\Phi(z,t) + \left(U_{solid}(z) + U_{hole}(z) - iU_\Gamma(z) + \mathcal{E}_{IR}(t)U_{IR}(z) - \hbar\omega\right)\Phi(z,t)$$
$$+ i\,A_0(t)\frac{\partial}{2\partial z}\Phi_0(z),$$

(S13)

where the velocity gauge and length gauge are used for EUV excitation and the interaction with the IR field, respectively. In Eq. S13, at variance with Eq. S11, only the absorption of one EUV photon is taken into account in the last term of this equation. The advantage of the rotating wave approximation (RWA) is that it does not refer to a particular intensity of the EUV pulse, which is factored out, and allows one to use larger time steps in the numerical wave packet propagation. Importantly, only the kinetic energy E of the ejected electron is relevant and hence within the RWA the exact energy ε_0 of the initial state $\Phi_0(z)$ is irrelevant.

The potential term in Eq. S13 comprises the jellium type potential of the solid U_{solid}, the screened electron-hole (e-h) interaction U_{hole} of the propagating photoelectron with the remaining hole, an optical potential U_Γ that accounts for inelastic electron scattering in the bulk, which determines the inelastic mean free path of electrons in the solid, and the potential term U_{IR} arising from the IR streaking field. The latter is modulated by the time evolution of the IR field $\mathcal{E}_{IR}$. The last term accounts for EUV excitation from the initial state Φ_0 with A_{EUV} as envelope of the EUV pulse vector potential.

The surface of the solid is assumed to be illuminated by an extreme ultra-violet (EUV) pulse with frequency $\omega_{EUV} \approx 91$ eV and duration 0.5 fs. This pulse is accompanied by an infrared (IR) laser pulse with frequency $\omega_{IR} = 1.55$ eV and intensity $P = 2 \cdot 10^{11}$ W cm^{-2}. The time of arrival of EUV pulse with respect to the IR pulse is varied and dependence of the electron energy spectrum on this time is an object of the study. The fields in incident pulses are assumed to be linearly polarized along the surface normal (the z-axis is directed along this normal from the surface to vacuum, $z = 0$ gives the position of the topmost Se layer). The EUV pulse ionizes atoms in bulk and the yield of electrons ejected along the surface normal is investigated.

2.2.1 Jellium type potential for WSe₂ solid

The impact of the solid on the photoelectron wave is taken into account using a jellium-type potential U_{solid} (Fig. S4). The potential step at the surface reflects the inner potential U_{IP} of WSe$_2$ of 14.5 eV (14). The choice of a jellium-type potential is based on the conception that the photoelectron in the continuum is not significantly influenced by the presence of the lattice in the solid. The value of the inner potential was confirmed by calculating time-reversed low energy electron diffraction (LEED) states (41) for WSe$_2$, which reflects the impact of the semi-infinite lattice on the photoemission state within the one step model of photoemission (42, 43). For the photoelectron kinetic energies considered here the emission is dominated by a free-electron-like

band with an effective mass of 1.08 m_e (see Fig. S7) and thus the choice of a jellium-type potential is plausible. The 8% change of effective mass leads to a 4% increase of the photoemission delays, that is in the order of 1 as and thus the effect is neglected in Eq. S13. With these data we have modeled the potential acting on the ejected electron in the bulk as follows:

$$U_{solid}(z) = \frac{U_{IP}}{2}\left(-1 + \tanh\left(\frac{z-z_s}{2}\right)\right), \tag{S14}$$
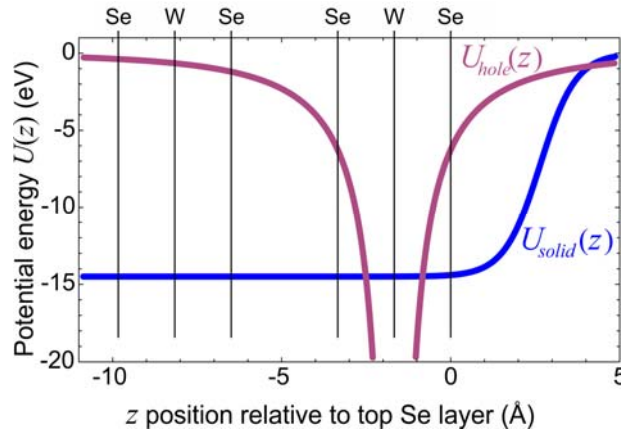
with $z_s = 0.25$ nm.

Fig. S4. Potentials used in 1D TDSE simulations of photoelectron propagation in WSe₂. *Static 1D potential contributions for 1D TDSE simulation of electron wave packet propagation. The jellium-type potential U_{Solid} is shown as blue line. The potential step height at the surface corresponds to the inner potential $U_{IP} = 14.5$ eV of WSe₂ as it was determined by photoemission spectroscopy (14). The interaction of the emitted photoelectron with the remaining hole is represented by a screened (screening length $\mu = 5$ Å) and regularized Coulomb potential (pink line) in this case shown for photoemission from the W atom in the top layer.*

2.2.2 Electron-hole interaction during photoemission

In contrast to free atoms the interaction of the emitted photoelectron with the remaining photohole is screened. Still for propagation over a distance given by the screening length the photoelectron feels the presence of the positive charge and is thus slowed down. This effect is accounted for by U_{hole} (Fig. S4), i.e. a 1D Yukawa potential with 5 Å screening length and a soft core parameter (44) $a = 0.15$ Å that regularizes the r^{-1} pole at the position of the atom from which the photoelectron originates. The potential $U_{hole}(z)$ arising from the interaction between the positively charged core and the electron ejected from the state localized on the atom positioned at z_0 is represented by

$$U_{hole}(z) = -\frac{\exp\left(-|z-z_0|/\mu\right)}{\sqrt{(z-z_0)^2 + a^2}} \ , \tag{S15}$$

where the screening parameter μ was set to 0.5 nm. The regularization of the Coulomb potential with parameter $a = 0.015$ nm has been introduced for computational reason. In the 1D TDSE simulation each atomic layer along the z-axis is treated separately and $U_{hole}(z)$ is shifted accordingly.

2.2.3 Calculation of IR electric field distribution at a vicinity of the WSe₂ surface

The atomic scale variation of the IR streaking field at the interface determines the photoelectron streaking. Fresnel optics rely on an abrupt interface between two homogeneous media and it is not defined where this interface is located on an atomic scale. To avoid this uncertainty in modeling streaking at an interface we rely on *ab-initio* methods to derive the dielectric response. To determine the spatial distribution of the electric field induced by an external field of IR laser, we employed time-dependent density functional theory (TDDFT) (*45*), where the central quantity is the dynamical density response function $\chi(\mathbf{r},\mathbf{r}',\omega)$ of an interacting electron system. The *ab-initio* treatment of WSe₂ is based on the known crystal structure reported in literature (*46, 14*). Within the linear response theory, $\chi(\mathbf{r},\mathbf{r}',\omega)$ determines the electronic density $n^{\mathrm{ind}}(\mathbf{r},\omega)$ induced in the system by an external potential $V^{\mathrm{ext}}(\mathbf{r}',\omega)$ according to

$$n^{\mathrm{ind}}(\mathbf{r},\omega) = \int dz' \, \chi(\mathbf{r},\mathbf{r}',\omega) \, V^{\mathrm{ext}}(\mathbf{r}',\omega) \ . \tag{S16}$$

In the framework of TDDFT, $\chi(\mathbf{r},\mathbf{r}',\omega)$ is a solution of the integral equation

$$\chi(\mathbf{r},\mathbf{r}',\omega) = \chi^0(\mathbf{r},\mathbf{r}',\omega) + \int d\mathbf{r}_1 \int d\mathbf{r}_2 \, \chi^0(\mathbf{r},\mathbf{r}_1,\omega) \, [v_c(\mathbf{r}_1,\mathbf{r}_2) + K_{\mathrm{XC}}(\mathbf{r}_1,\mathbf{r}_2,\omega)] \, \chi(\mathbf{r}_2,\mathbf{r}',\omega) \tag{S17}$$

with $\chi^0(\mathbf{r},\mathbf{r}',\omega)$ being the response function (polarizability) of the non-interacting Kohn-Sham electrons. Here $v_c(\mathbf{r}_1,\mathbf{r}_2)$ is the bare Coulomb potential and $K_{\mathrm{XC}}(\mathbf{r}_1,\mathbf{r}_2,\omega)$ accounts for the exchange-correlation (XC) effects for which in this work we used the random-phase approximation, i.e. setting it to zero. For description of the electronic structure and excitation spectrum of the WSe₂(0001) surface we employ a three-dimensional model considering a repeated-slab geometry with the WSe₂(0001) slabs separated by vacuum intervals. Such geometry allows us to express all the quantities in a matrix form in the basis of the reciprocal lattice vectors $\mathbf{G}$. The slab consists of 6 W and 12 Se atomic layers using the bulk lattice parameters. The vacuum interval corresponds to the three lattice parameters along the c lattice direction, i.e. parallel to the surface normal.

The self-consistent electronic band structure of such a system was obtained employing the norm-conserving non-local pseudopotentials (*47*) for description of the electron-ion interaction. The local-density approximation was chosen for the exchange-correlation potential using the

Perdew-Zunger parametrization (*48*) of the exchange-correlation potential of Ceperley and Alder (*49*). The resulting one-particle energies and wave-functions were employed in the evaluation of $\chi^0_{\mathbf{GG'}}(\mathbf{q},\omega)$ matrix according to

$$\chi^0_{\mathbf{GG'}}(\mathbf{q},\omega) = \frac{2}{S}\sum_{\mathbf{k}}^{2BZ}\sum_{n}^{occ}\sum_{n'}^{unocc}\frac{f_{n\mathbf{k}}-f_{n'\mathbf{k}+\mathbf{q}}}{E_{n\mathbf{k}}-E_{n'\mathbf{k}+\mathbf{q}}+(\omega+i\eta)}\langle\phi_{n\mathbf{k}}\,|\,e^{-i(\mathbf{q}+\mathbf{G})\mathbf{r}}\,|\,\phi_{n'\mathbf{k}+\mathbf{q}}\rangle\langle\phi_{n'\mathbf{k}+\mathbf{q}}\,|\,e^{i(\mathbf{q}+\mathbf{G'})\mathbf{r}}\,|\,\phi_{n\mathbf{k}}\rangle. \quad \text{(S18)}$$

These calculations were carried out using a 120×120 $\mathbf{k}_{\parallel}$ grid for the sampling over the two-dimensional Brillouin zone. All the energy bands with energies up to 20 eV above the Fermi level were included. In order to save computational time, in the expansion of $\chi^0_{\mathbf{GG'}}$ we employed only $\mathbf{G}=(0,0,G_z)$ vectors, i.e. the local-field effects in the direction perpendicular to the surface were taken into account only. Nevertheless, all important three-dimensional effects are accounted for in the evaluation of $\chi^0_{\mathbf{GG'}}$ via inclusion of the one-particle wave functions in the evaluation of the matrix elements.
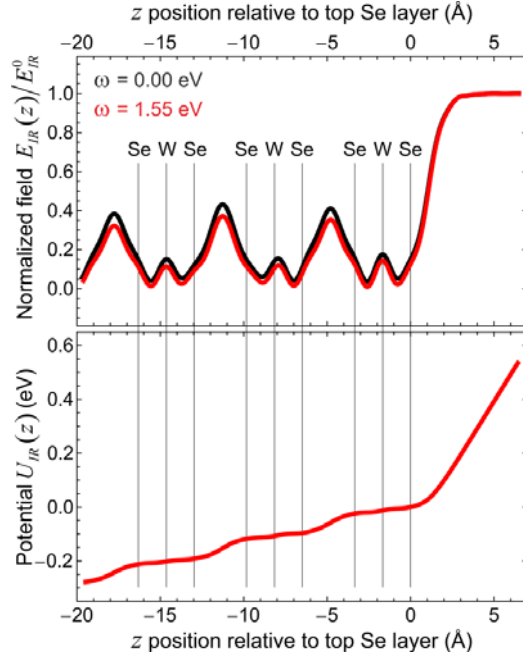

Fig. S5. IR Streaking field and related potential U_{IR} at the WSe$_2$-vacuum interface. *Time-dependent streaking field E_{IR} (upper panel) and corresponding potential U_{IR} (lower panel) reflecting the perturbation due to the IR streaking field. The field screening at the interface and the penetration into the bulk is derived from ab-initio electronic structure calculations for WSe$_2$. The actual potential distribution corresponds to external normal field strength of 0.1 V Å^{-1}. The vertical dashed lines indicate the position of the different atomic layers in WSe$_2$.*

Having obtained the $\chi^0_{\mathbf{GG'}}(\mathbf{q}_{\parallel},\omega)$ for the smallest $\mathbf{q}_{\parallel}$ vectors, we calculated the corresponding induced density distribution $n^{\text{ind}}(z,\mathbf{q}_{\parallel},\omega)$ according to Eq. S16. Subsequently, on

base of these data the corresponding induced potential $V^{\text{ind}}(z,\mathbf{q}_{\|},\omega)$ for such $\mathbf{q}_{\|}$'s was obtained. The normal electric field distribution was calculated numerically according to $E(z,\omega) = \Delta V^{\text{ind}}(z,\mathbf{q}_{\|},\omega)/\Delta z$. The results of computation of the IR electric field screening and the relevant for the present study z-dependence of the corresponding potential $U_{IR}(z)$ are plotted in Fig. S5.

2.2.4 Calculation of the inelastic mean free path (MFP) of excited electrons

One essential property of the solid which determines the streaking delay is the electron mean free path (MFP) directly related to the imaginary potential $-iU_{\Gamma}(\mathbf{r})$ and the inelastic lifetime t_{inel} of the electrons in the bulk. These quantities are related to each other and determine the dependence of the yield of electrons ejected from various layers of the solid for a given kinetic electron energy due to the electron-electron inelastic scattering.

The MFP of electrons follows roughly the universal curve (50). The kinetic energies of the emission channels studied here lie close to the minimum of the universal curve, i.e. the inelastic MFP is in the order a few Å. The universal curve provides just qualitative information and the MFP varies significantly between different systems. Since experimental values are not available for WSe$_2$ we here rely on theoretical values derived from *ab-initio* electronic structure calculations. The one-electron states, obtained in the first-principles band structure calculations of a bulk WSe$_2$ crystal, are characterized by energy $\varepsilon_{n\mathbf{k}}$ and a wave function $\psi_{n\mathbf{k}}(\mathbf{r})$, where n and $\mathbf{k}$ are band numbers and wave vectors, respectively. The experimental conditions imply that the electron emission normal to the surface should be considered only. This restricts the relevant electronic states to the states only along the $\Gamma - A$ symmetry direction of the Brillouin zone (BZ). The lifetime of electron states for all energy bands in this direction was calculated. For evaluation of $\varepsilon_{n\mathbf{k}}$ and $\psi_{n\mathbf{k}}(\mathbf{r})$ in bulk WSe$_2$ we used a self-consistent pseudopotential method with the ion-electron interaction described by a norm-conserving pseudopotential (47). To describe the exchange-correlation potential the local-density approximation was employed (48, 49).

The width $\Gamma_{\mathbf{n}k}$ of an electron state is related to the imaginary part of the self-energy $\Sigma_{n\mathbf{k}}$ via

$$\Gamma_{n\mathbf{k}} = -2 \cdot \text{Im}\Sigma_{n\mathbf{k}}, \tag{S19}$$

where $\text{Im}\Sigma_{n\mathbf{k}}$ is evaluated as the projection of $\text{Im}\Sigma(\mathbf{r},\mathbf{r}',\varepsilon_{n\mathbf{k}})$ onto the one-electron state $\psi_{n\mathbf{k}}(\mathbf{r})$ (51, 52)

$$\text{Im}\Sigma_{n\mathbf{k}} = \int \psi_{n\mathbf{k}}^{*}(\mathbf{r})\,\text{Im}\Sigma(\mathbf{r},\mathbf{r}',\varepsilon_{n\mathbf{k}})\psi_{n\mathbf{k}}(\mathbf{r}')\,d\mathbf{r}\,d\mathbf{r}'. \tag{S20}$$

The self-energy $\Sigma(\mathbf{r},\mathbf{r}',\varepsilon_{n\mathbf{k}})$ is calculated within the *GW* approximation of many-body theory (51), with *W* being the screened Coulomb interaction, and with the Green function *G* replaced by the non-interacting Green function. Thus, for $\text{Im}\Sigma$ one obtains

$$\text{Im}\Sigma(\mathbf{r},\mathbf{r}',\varepsilon_{n\mathbf{k}}) = \sum_{m,\mathbf{q}}^{\varepsilon_F < \varepsilon_{m\mathbf{q}} < \varepsilon_{n\mathbf{k}}} \psi_{m\mathbf{q}}^*(\mathbf{r})\,\text{Im}W(\mathbf{r},\mathbf{r}',\varepsilon_{n\mathbf{k}} - \varepsilon_{m\mathbf{q}})\psi_{m\mathbf{q}}(\mathbf{r}'), \tag{S21}$$

where the sum is extended over the final states $\psi_{m\mathbf{q}}(\mathbf{r})$ with energy $\varepsilon_{m\mathbf{q}}$, ε_F is the Fermi energy, and $W(\mathbf{r},\mathbf{r}',\omega)$ is the screened interaction given by

$$W(\mathbf{r},\mathbf{r}',\omega) = \int \epsilon^{-1}(\mathbf{r},\mathbf{r}'',\omega)V(\mathbf{r}'' - \mathbf{r}')\,d\mathbf{r}'' \ . \tag{S22}$$

Here, $\epsilon^{-1}(\mathbf{r},\mathbf{r}'',\omega)$ and $V(\mathbf{r})$ represent the inverse dielectric function and the bare Coulomb potential, respectively. Within the RPA the Fourier transform of the dielectric matrix $\epsilon_{\mathbf{GG}'}^{-1}(\mathbf{k},\omega)$ is related to the density-response function $\chi_{\mathbf{GG}'}(\mathbf{k},\omega)$ via

$$\epsilon_{\mathbf{GG}'}^{-1}(\mathbf{k},\omega) = \delta_{\mathbf{GG}'} + \chi_{\mathbf{GG}'}(\mathbf{k},\omega)V_{\mathbf{G}'}(\mathbf{k}) \ , \tag{S23}$$

where $V_{\mathbf{G}}(\mathbf{k}) = 4\pi / |\mathbf{k} + \mathbf{G}|^2$ is the Fourier transform of the bare Coulomb potential.

For evaluation of χ we solve Eq. S17 employing χ^0 obtained according to the expression similar to Eq. S18. In this case the vectors $\mathbf{k}$ and $\mathbf{q}$ are in a three-dimensional BZ. Sampling over the BZ was performed on the 72x72x18 $\mathbf{k}$ mesh. We included all the states with the energies up to 125 eV above the Fermi level. In the expansion of χ^0, χ, and ϵ^{-1} we employed 76 $\mathbf{G}$ vectors.

Using Fourier transforms for all quantities in Eq. S21, we obtain

$$\Gamma_{n\mathbf{k}} = 2 \sum_{m\mathbf{q}}^{\varepsilon < \varepsilon_{m\mathbf{q}} < \varepsilon_{n\mathbf{k}}} \sum_{\mathbf{G},\mathbf{G}'} \text{Im}W_{\mathbf{GG}'}(\mathbf{k} - \mathbf{q},\varepsilon_{n\mathbf{k}} - \varepsilon_{m\mathbf{q}})B_{nm}^*(\mathbf{k},\mathbf{q},\mathbf{G})B_{nm}(\mathbf{k},\mathbf{q},\mathbf{G}'), \tag{S24}$$

where $W_{\mathbf{GG}'}$ is the Fourier transform of the screened interaction $W(\mathbf{r},\mathbf{r}',\omega)$ and $B_{nm}(\mathbf{k},\mathbf{q},\mathbf{G})$ is

$$B_{nm}(\mathbf{k},\mathbf{q},\mathbf{G}') \equiv \sum_{\mathbf{G}'} a_n^*(\mathbf{k} + \mathbf{G} + \mathbf{G}')a_m(\mathbf{q} + \mathbf{G}') \ . \tag{S25}$$

Here $a_m(\mathbf{q} + \mathbf{G})$ are the expansion coefficients of the wave function $\psi_{n\mathbf{k}}(\mathbf{r})$. In Eq. S24 summing has been performed over the $\mathbf{q}$ points on a 24x24x12 mesh in the BZ.

When $\Gamma_{n\mathbf{k}}$ is computed, the life time $\tau_{n\mathbf{k}}$ of the corresponding state can be obtained as

$$\tau_{n\mathbf{k}} = \Gamma_{n\mathbf{k}}^{-1} \ . \tag{S26}$$

Knowing the life time, one can obtain the mean free path by multiplication of this time by the transport velocity (27, 53), which equals to $\sqrt{2E_{bulk}}$ in the case of high enough electron energy in the bulk. The dependencies of these quantities on the electron energy in vacuum are plotted on Fig. S6. For all emission channels the MFP lies between 5-6 Å. Note that the MFP is much smaller than the EUV penetration depth ($\approx$ 5 nm for 85° incidence angle) (54) and thus a homogeneous EUV excitation profile is assumed.

Here we construct the Bloch waves related to the escape of the photoelectron to the vacuum. We are interested in the dependence of the electron energy E on the Bloch vector component $k^\perp$ perpendicular to the surface. Following the one-step theory of photoemission (42, 43), which

reduces the stationary photoemission to the optical transition from an initial state to a time-reversed low energy electron diffraction (LEED) state, we have performed the calculation of LEED for the WSe$_2$(0001) surface. Importantly, within this theory the inelastic scattering of electrons in the bulk is taken into account via the imaginary contribution $-iU_\Gamma(E)$ to the crystal potential inside the solid. The optical potential U_Γ is related to the inverse lifetime of the electron as $U_\Gamma = \Gamma/2$. The absorbing potential makes the Hamiltonian non-Hermitian, and the LEED functions decay exponentially into the crystal. Thus, for real E all $k_\lambda^\perp$ become complex. The present calculation is performed with the energy dependent decay rate $\Gamma(E)$ shown in Fig. S6.
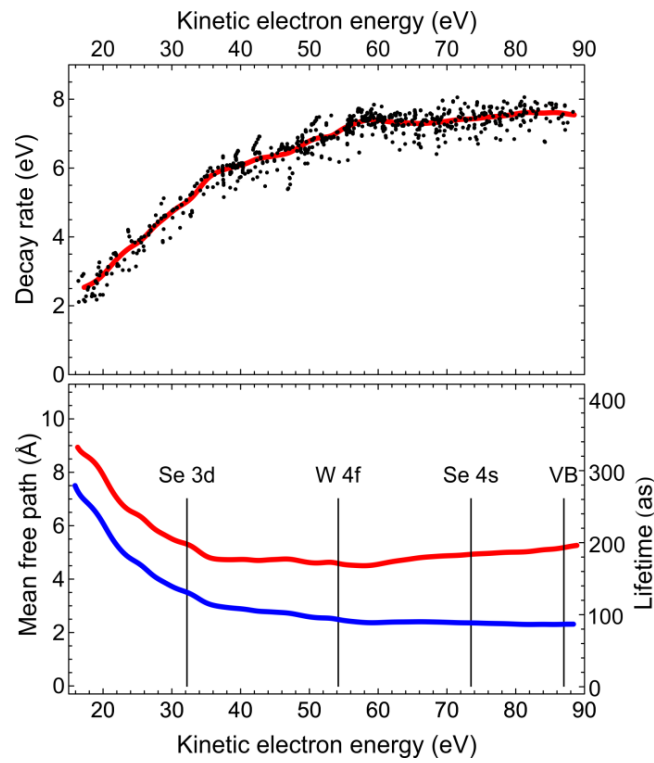

Fig. S6. Excited electron decay rate and inelastic mean free path. *The upper panel shows the calculated decay rate $\Gamma(E)$ of the electron states as black points and their averaged data as red line. In the lower panel the corresponding inelastic electron mean free path is shown (red line). The inelastic mean free path (red line) and the corresponding excited electron lifetime (blue line) as derived from ab-initio electronic structure calculations are shown in the lower panel as function of the electron kinetic energy measured relative to the vacuum level. The vertical lines indicate the kinetic energies at which the corresponding photoemission peaks appear for EUV photoemission at 91 eV photon energy.*

The points in Fig. S7 are obtained as solutions $k_\lambda^\perp(E)$ of the inverse band structure problem, i.e., the Bloch solutions of the Schrödinger equation for the energy E with complex Bloch vectors $k_\lambda^\perp$ (abscissa is the real part of $k^\perp$). The solutions $k_\lambda^\perp$ for a given energy E were generated using the extended LAPW $\mathbf{k} \cdot \mathbf{p}$ method (linear 6 augmented plane waves), which reduces the inverse band structure problem to a matrix eigenvalue problem (41). The scattering solution is then obtained as a linear combination of the partial waves (Bloch waves) (55).
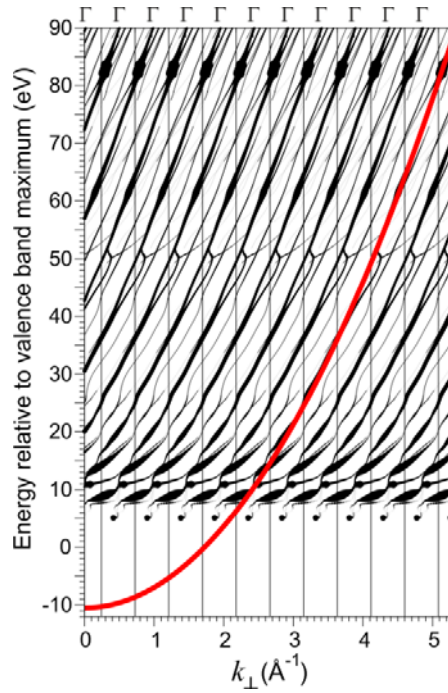

Fig. S7. Continuum band structure of WSe$_2$ for the emission from the (0001) surface in the repeated zone scheme. *The energy dependent optical potential $-iU_\Gamma(E)$ is included. Several conducting branches are shown; their relative contributions to the LEED function are indicated by the size of the symbols. The red line is the parabola $E(k) = U_{IP} + (\hbar k)^2/2m^*$ with $m^* = 1.08\ m_e$ and $U_0 - E_{vac} = -10.5$ eV. The $k_\lambda^\perp(E)$ lines constitute the so-called complex band structure (56) of the semi-infinite crystal. To highlight the waves that most strongly contribute to the LEED state and are, at the same time, relevant to the bulk band structure, we choose the size of the symbol in Fig. S7 to be proportional to the current carried by the individual wave multiplied by the corresponding mean free path $2(\text{Im}k_\lambda^\perp)^{-1}$. Generally, the contributions of the branches vary with energy, but one can easily notice one line with a persistently large contribution over the whole energy range. It is rather accurately fitted by the parabola $E(k) = U_{IP} + (\hbar k)^2/2m^*$ with the effective mass $m^* = 1.08\ m_e$ and inner potential*

$U_{IP} = -10.5\ eV$, *see Fig. S7. This agrees well with the nearly-free-electron estimate from angle-resolved photoemission measurements (14): $m^* = 1.05 \pm 0.05\ m_e$ and $U_{IP} = -14.5 \pm 0.5\ eV$ for the inner potential of WSe$_2$ (the work function of WSe$_2$ is 5.2 eV according to (57, 58)).*

However, the results in Fig. S7 are obtained with a one-particle Hamiltonian in the local density approximation. For high-energy states this approximation is known to lead to underestimated energies of the quasiparticles by about 1 eV or more. This energy shift grows with energy, and it is different for different materials, see Refs. (*59–61*). Presently, this correction can only be obtained from an experiment, so here it is ignored.

2.2.5 *Derivation of the initial electron wave functions*

As a final step the initial state wave functions $\Phi_0(z)$ for each emission channel are required to numerically integrate Eq. S13. These states were derived from orbitals calculated using density functional theory (DFT) calculations. In contrast to the *ab initio* treatment dielectric response, inelastic mean free path, and the continuum band structure described in the previous subsections the determination of initial states for the 1D TDSE model is based on molecular orbitals for the compounds W$_3$Se$_6$ and W$_6$Se$_{12}$ that mimic a single and a double layer of WSe$_2$. The corresponding molecular orbitals for W$_3$Se$_6$ and W$_6$Se$_{12}$ have D_{3h} and D_{3d} symmetries, respectively. The wave functions were extracted from a formatted checkpoint file generated by the Gaussian09 (*62*) package using the M06 functional (*63*) and the DZP basis set (*64, 65*). In addition, the relativistic effects have also been taken into account considering the Douglas-Kroll-Hess second order approach (*66–69*).

The numerical integration of the molecular orbital densities (valence band, Se 4s, W 4f, and Se 3d) in the *xy*-planes as functions of z were evaluated using an integration grid of 15 million points (*70, 71*). Overall, they were evaluated for a total of 90 and 175 molecular orbital densities for the W$_3$Se$_6$ and W$_6$Se$_{12}$ molecular structures, respectively. From the states with non-vanishing projection magnitude Φ_0^{proj} were selected since only these states contribute to photoemission normal to the surface. The obtained projected initial state wave functions corresponding to the photoemission channels observed experimentally are plotted in Fig. S8 . One can see that the wave functions are well localized inside the dimer. Note that the valence band states have different energies in the range of 10 eV - 7 eV below the vacuum level.
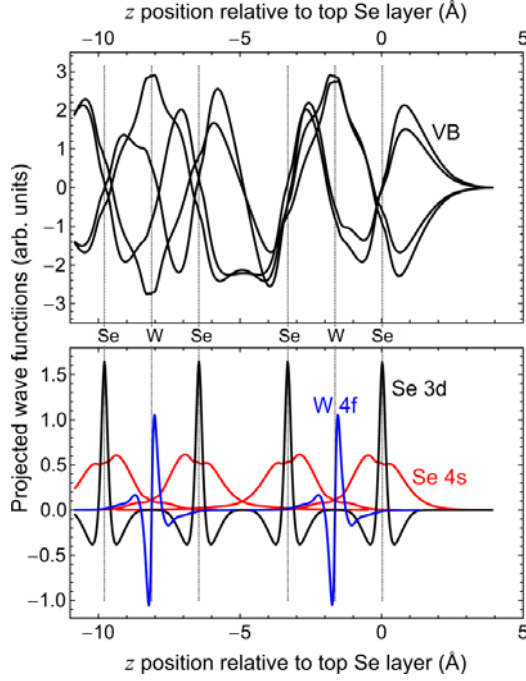
Fig. S8. Initial state wave functions $\Phi_0(z)$ ***for solving the 1D TDSE.*** *The upper panel shows four different valence band states. In the lower panel the Se 3d (black), Se 4s (red), and W 4f initial states (blue) are displayed. Note that for the latter states for each layer an individual initial state is used in the 1D TDSE simulation.*

2.2.6 *Photoemission delays derived from solving the 1D TDSE*

Eq. S13 was solved using the split-propagation approach (*72*) (for details about the implementation see Refs. (*11, 12*)). The system was considered on the mesh with $N = 32768$ nodes on the interval $[-4.5 \text{ nm}, 201 \text{ nm}]$. The time step for numerical propagation is $dt = 0.48$ as. The energy distribution was obtained from a Fourier transform of the wave packet for a propagation time well after the IR pulse termination, i.e. when the wave packet is definitely localized far from the solid-vacuum interface. Based on the so calculated photoelectron kinetic energy spectra for different delay $t_{IR} - t_{EUV}$ between IR and EUV pulse the theoretical streaking spectrograms were computed (Fig. S9A). The following procedure to determine the relative delay between the streaking spectrograms for the different emission channels was employed: For each emission channel the center of energy of the photoelectron kinetic energy distribution (COE) was determined as function of the delay $t_{IR} - t_{EUV}$. The corresponding temporal shift of these delay-dependent COEs relative to the time-dependence of the vector-potential of the IR pulse $A_{IR}(t) = \int_t^\infty \mathcal{E}_{IR}(t') \, dt'$ are a measure of the total photoemission delay τ_d^j of the corresponding photoemission channel $j = \text{VB}, \text{Se 4s}, \text{W 4f}, \text{Se 3d}$. τ_d^j is positive when the j-th COE curve is shifted to smaller delay $t_{IR} - t_{EUV}$. In this case the electrons emitted from the j-th initial state are delayed in solid by time τ_d^j. The lower index d indicates that the 1D TDSE

propagation is performed for a double-layer of WSe$_2$ monolayers. As pointed out in the following the delay correction caused by photoemission from deeper layers can be accounted for quantitatively.

In computations, we have considered the initial wave functions nested at the first 6 atomic layers of WSe$_2$, i.e. the two uppermost van der Waals layers. However, it is possible to quantitatively account for the effect of emission from deeper atomic layers using the following procedure: The effect due to the infinite number of WSe$_2$ layers can be directly evaluated by

$$\tau_\infty^j = \frac{\sum_{n=0}^{\infty}\left(\tau_d^j + n\,L_d\big/v^j\right)\exp(-n\,L_d/\lambda)}{\sum_{n=0}^{\infty}\exp(-n\,L_d/\lambda)} = \tau_d^j + \frac{\lambda}{v^j\left(\exp(L_d/\lambda)+1\right)}, \qquad \text{(S27)}$$

where τ_d^j and τ_∞^j are the times to reach the surface for the electron ejected from the j-th emission channel related to initial states in the WSe$_2$ dimer or the infinite chain of dimers, $L_d = 1.296$ nm is the spatial period of the dimer chain, λ is the inelastic MFP taken for the corresponding kinetic energies from the relation shown in Fig. S6, and $v^j = \sqrt{2\,E_{bulk}^j}$ is the velocity of the ejected electron into channel j inside the bulk.
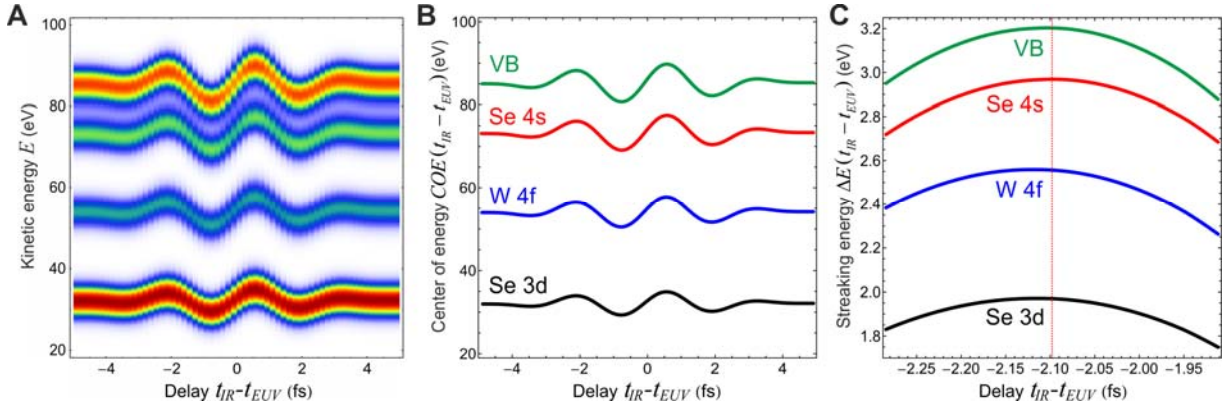

Fig. S9. 1D TDSE streaking spectrogram. (A) Streaking spectrogram derived from 1D TDSE calculation following the procedure described in the text. (B) Variation of the center of energy for the four different emission channels VB, Se 4s, W 4f, and Se 3d as function of the delay between the IR pulse and the EUV pulse. (C) Streaking energy $\Delta E\left(t_{IR} - t_{EUV}\right) = COE\left(t_{IR} - t_{EUV}\right) - COE\left(\infty\right)$ as function of the delay between the IR pulse and the EUV pulse zoomed in on the first maximum. The vertical dashed line is centered at the maximum of the Se 4s signal. From the relative shift of the COE curves the theoretical relative photoemission delays are determined.

Experimentally measured are only the relative delays between any pair of such delays. In the following we always refer to the delay difference $\Delta t_{j-\text{Se}4s}$ with respect to the photoemission

delay of the Se 4s photoelectrons defined as $\Delta t_{j-\mathrm{Se4s}} = \tau_\infty^j - \tau_\infty^{\mathrm{Se4s}}$. Accordingly, these values yield the following relative delays: $\Delta t_{\mathrm{VB-Se4s}} = 6$ as, $\Delta t_{\mathrm{Se3d-Se4s}} = 15$ as, and $\Delta t_{\mathrm{W4f-Se4s}} = 24$ as, as they are listed in Tab. 1 of the main manuscript and are obtained as the sum of the values listed in Tab. S3 in the 2$^{\mathrm{nd}}$ and 3$^{\mathrm{rd}}$ column (Section 3).

3   Summary of theoretically derived relative photoemission delays

Finally the various theoretically derived delays summarized in Tab. S3 are combined and compared to the experimentally determined values. The second column in Tab. S3 list the delays derived from 1D TDSE simulation of photoemission from a double layer of WSe$_2$. Se 4s emission is first. With 6 as, 14 as, and 22 as delay the emission form the VB, Se 3d, and W 4f, respectively, occur. Here the effect of emission from deeper layers in the bulk of WSe$_2$ is neglected and the values have to be corrected according to Eq. S27, i.e. by the values listed in the 3$^{\mathrm{rd}}$ column. The 4$^{\mathrm{th}}$ and 5$^{\mathrm{th}}$ column summarize the intra-atomic delays derived by the non-relativistic Hartree-Slater approach and the relativistic MCDF method. Consistently both methods add a delay that increases with the initial state angular momentum. Note that no intra-atomic corrections can be derived for the valence band states since the wave function is no longer localized at a particular atom. The theoretically predicted total delay is listed in the 6$^{\mathrm{th}}$ column. The values obtained with both intra-atomic corrections agree with the experimental values within the uncertainties.

Tab. S3. Comparison between experimental and theoretical photoemission delays.

Initial state	$\Delta t_{j-\mathrm{Se4s}}^{\mathrm{1D\,TDSE}}$	$\tau_\infty^j - \tau_d^j$ (eq. S27)	τ_{eff}^{HS} (eq. S8)	$\tau_{\mathrm{eff}}^{MCDF}$ (eq. S10)	Full delay HS / MCDF	Exp. results
VB	6	0	-	-	12 / 12	12±10
Se 4s	0	0	-6	-6	0	-
W 4f	22	2	14	6	44 / 36	47±14
Se 3d	14	1	8	4	29 / 25	28±10

The results of computations of delays, in attoseconds. The 1st column: initial states for the considered emission channels; the 2nd column: the propagation delays obtained by solving the 1D TDSE for electron emission from the first two WSe$_2$ layers; the 3rd column: delay corrections due to emission from deeper WSe$_2$ layers; the 4th column: the EWS delays obtained with HS potential; the 5th column: the delays obtained from multi configurational Dirac-Fock approximation; the 6th column: the full delays calculated relative to Se 4s emission; the 7th column: the corresponding experimental results.